

TECHNISCHE HOCHSCHULE KÖLN

University of Applied Sciences

Cologne Institute for Renewable Energy

Degree: Bachelor Erneuerbare Energien

Bachelor Thesis

**Spectral characterisation of high temperature
solar absorber coatings**

Bachelor thesis submitted by: Leslie Herding

Student ID: 11090896

1st examiner: Prof. Dr. rer. nat. Volker Nickich

2nd examiner: Dipl.-Ing. Simon Caron

Date of issue: 19.12.2017

Date of submission: 20.02.2018

Register-N°: BA EE 39/18

In cooperation with:

German Aerospace Centre

Institute of Solar Research

Plataforma Solar de Almería, Tabernas (Spain)



DLR

**Deutsches Zentrum
für Luft- und Raumfahrt**

Spectral characterisation of high temperature solar absorber coatings

Register-N°: BA EE 39/18

Submitted by Leslie Herding

Cologne Institute for Renewable Energy

Date of submission: 20.02.2018

1st examiner: Prof. Dr. rer. nat. Volker Nickich

2nd examiner: Dipl.-Ing. Simon Caron

Keywords: concentrating solar power, spectrophotometry, round robin, solar absorptance, thermal emittance, solar absorber coatings

Abstract

In the course of the Raiselife project, four solar absorber coatings are to be evaluated after thermal cycling at a dish facility. One key parameter is the thermal emittance. Optical measurements carried out at PSA show a deviation between two complementary spectrophotometers. Different approaches for the mismatch correction are applied. After the successful correction, a new measurement routine following DIN EN ISO 22795-3 is defined and the corrected values are evaluated with a round robin campaign. The standard deviation of thermal emittance values determined by different participating laboratories can be reduced by implementing a common processing of spectral data. The postprocessed DLR/CIEMAT value deviates around 2.1 % from the mean value determined within the round robin campaign. A new calibrated reference standard promises a further reduction of the deviation and hence an improvement in the absorber coatings' thermal efficiency characterisation.

Spektrale Charakterisierung von Hochtemperaturabsorberbeschichtungen

Registernummer: BA EE 39/18

Eingereicht von Leslie Herding

Cologne Institute for Renewable Energy

Abgabedatum: 20.02.2018

Erstprüfer: Prof. Dr. rer. nat. Volker Nickich

Zweitprüfer: Dipl.-Ing. Simon Caron

Keywords: konzentrierende Solarthermie, Spektrophotometrie, Ringversuch, solarer Absorptionsgrad, Wärmeemissionsgrad, Solarabsorberbeschichtungen

Kurzfassung

Im Zuge des Raiselife Projekts werden vier Absorberbeschichtungen mit Hilfe von thermischen Zyklen bewertet. Ein wichtiger Parameter ist der Wärmeemissionsgrad. Optische Messungen in den Laboren der PSA zeigen eine Abweichung zwischen zwei komplementären Spektrophotometern. Verschiedene Ansätze zur Korrektur des Fehlers werden angewendet. Nach der erfolgreichen Behebung des Fehlers wird eine neue Messroutine nach DIN EN ISO 22795-3 abgeleitet und die korrigierten Werte werden durch einen Ringversuch evaluiert. Die Implementierung einer allgemeinen Methodik zur spektralen Datenverarbeitung ermöglicht eine Reduzierung der Standardabweichung des Wärmeemissionsgrads zwischen den teilnehmenden Laboren. Der nachbearbeitete DLR/CIEMAT Wert zeigt eine Abweichung von rund 2.1 % zum im Ringversuch bestimmten Mittelwert. Ein neuer kalibrierter Referenzstandard verspricht eine weitere Minimierung der Abweichung und somit eine Verbesserung der Charakterisierung der thermischen Effizienz der Absorberbeschichtungen.

Table of Contents

Abstract	I
Kurzfassung	II
List of figures	IV
List of tables.....	V
List of abbreviations	VI
List of symbols and units	VII
List of physical constants	VIII
Glossary	IX
1 Introduction	1
2 State of the art	2
2.1 CSP plants	2
2.2 Solar cycling test bench	4
2.3 Optimisation potential.....	7
3 Optical characterisation	10
3.1 Spectrophotometry.....	11
3.2 Determination of optical properties	12
3.3 Round robin campaign	14
4 Calculation methods.....	17
4.1 Solar absorptance	17
4.2 Thermal emittance	19
5 Results and discussion	28
5.1 Solar absorptance	28
5.2 Thermal emittance	31
5.3 Discussion and improvements	43
6 Summary and outlook	52
7 Bibliography	54
8 Appendix	X
9 Declaration of Academic Honesty	XVII

List of figures

Figure 1 – Four main technologies for CSP plants [13]	3
Figure 2 – Temperature and flux profile of a thermal cycle [17]	6
Figure 3 – Temperature measurement principle [17].....	7
Figure 4 – Example of mismatch between spectral data	9
Figure 5 – ASTM G173-03 solar spectra [20]	10
Figure 6 – Ideal black body radiation at different temperatures.....	14
Figure 7 – Overview work steps solar absorptance	17
Figure 8 – UV-VIS-NIR spectral data provided by the project partners.....	18
Figure 9 – Overview work steps thermal emittance	20
Figure 10 – IR spectral data provided by the project partners.....	21
Figure 11 – Internal mismatch correction approaches.....	22
Figure 12 – Frontier FTIR integrating sphere measurement	23
Figure 13 – Deviation of Frontier FTIR measurement zoom in.....	23
Figure 14 – Overview of extrapolation approaches	26
Figure 15 – Overview: solar absorptance calculation approaches and their results	30
Figure 16 – Flow chart of solar absorptance data processing	31
Figure 17 – Post-processing approach 1 for Frontier FTIR data	32
Figure 18 – Post-processing approach 2 for Frontier FTIR data	33
Figure 19 – IR spectral data used within the round robin campaign.....	34
Figure 20 – Comparison of WS measurements with new measurement routine	35
Figure 21 – Comparison of black body reference data at 923 K	36
Figure 22 – Comparison of extrapolation methods	37
Figure 23 – Absolute comparison of extrapolation approaches.....	38
Figure 24 – Black body reference data (923K), zoom 0 to 5,000 nm	40
Figure 25 – Variation of end wavelength with extrapolation approach ISO	41
Figure 26 – Black body reference data (923 K), zoom 10,000 to 50,000 nm	41
Figure 27 – Overview: thermal emittance calculation approaches and their results	45
Figure 28 – Thermal emittance values at 923 K before and after processing	46
Figure 29 – Flow chart of thermal emittance data processing	47
Figure 30 – Flow chart of recommended post-processing.....	48
Figure 31 – Deviation of DLR/CIEMAT thermal emittance from round robin average	49
Figure 32 – Flow chart new measurement routine	50
Figure 33 – Overview lever positions used for new measurement routine	51
Figure 34 – Raiselife PERT chart lining out the workflows within the project [11].....	XI
Figure 35 – Difference between processed data of WS measurements	XII
Figure 36 – Frontier FTIR data and MATLAB smooth functions.....	XIII
Figure 37 – Overview Mindjet MindManager	XV
Figure 38 – Detailed view Mindjet MindManager.....	XVI

List of tables

Table 1 – Overview of modifications on dish test facility [17]	5
Table 2 – Parameters for calculating thermal efficiency and their optimisation potential	8
Table 3 – Round robin overview for solar absorptance	15
Table 4 – Round robin overview for thermal emittance	16
Table 5 – Solar absorptance round robin values	18
Table 6 – Wavelength ranges of solar absorptance calculation scenarios	19
Table 7 – Thermal emittance round robin values	21
Table 8 – Wavelength ranges of thermal emittance calculation scenarios	27
Table 9 – Comparison of weighted solar absorptances with reference values	28
Table 10 – Variation of the wavelength range for solar absorptance	29
Table 11 – Relative comparison of ISO extrapolation approach	38
Table 12 – Variation of start wavelength without extrapolation	39
Table 13 – Relative comparison of the 50,000 nm end wavelength scenario	42
Table 14 – Result of different calculation methods	43
Table 15 – Measurement and calculation processes of the round robin partners	44
Table 16 – Thermal efficiency parameters and their optimisation potential update	52
Table 17 – Thermal emittance of DLR/CIEMAT data with different MATLAB algorithms	XIII
Table 18 – Overview Project organisation with Microsoft Excel	XIV

List of abbreviations

Abbreviation	Meaning
AM	Air mass
avg	Average
CIEMAT	Centro de Investigaciones Energéticas, Medioambientales y Tecnológicas
CSP	Concentrated Solar Power
DLR	Deutsches Zentrum für Luft- und Raumfahrt (German Aerospace Centre)
DSLR	Digital Single Lens Reflex
EM	Electromagnetic
FTIR	Fourier-Transform Infrared
HTF	Heat Transfer Fluid
IR	Infrared
LCOC	Levelised Cost of Coating
LCOE	Levelised cost of Energy
MENA	Middle East and North Africa
NIR	Near Infrared
NIST	National Institute of Standards and Technology
OPAC	Optical Aging Characterization Laboratory
PSA	Plataforma Solar de Almería
PV	Photovoltaic
Raiselife	“Raising the Lifetime of Functional Materials for Concentrated Solar Power Technology”
stdev	Standard deviation
UV	Ultraviolet
VIS	Visible
WP	Work Package
WS	Working Standard

List of symbols and units

Symbol	Meaning	Unit
E	Exitance	W/m ² nm
Q	Flux	W/m ²
T	Temperature	K
ρ	Reflectance	-
$\sigma\%$	Percentage of Stefan-Boltzmann constant	%
τ	Transmission	-
G	Reference spectrum for solar direct normal irradiance	W/m ² nm
α	Absorptance	-
ε	Emittance	-
η	Efficiency	-
λ	Wavelength	nm

Index	Meaning
1050	Lambda 1050 spectrophotometer
abs	Absorber
avg	Average
BB	Black body
FTIR	FTIR spectrophotometer
hem	Hemispherical
meas	Measure
sol	Solar
std	Standard (reference)
th	Thermal
WS	Working standard

List of physical constants

Symbol	Name	Value	Unit
c	Speed of light	299,792,458	m/s
h	Planck constant	$6.626 \cdot 10^{-23}$	J*s
k	Boltzmann constant	$1.381 \cdot 10^{-23}$	J/K
σ	Stefan-Boltzmann constant	$5.670 \cdot 10^{-8}$	W/m ² K ⁴

All constants are defined according to the National Institute of Standards and Technology (NIST) Standard Reference Database [1].

Glossary

Term	Explanation
Absorptance	"The ratio of the absorbed radiant flux to the incident radiant flux." [2]
Air mass	"The air mass is defined as the ratio of the slant path length of the solar rays through the atmosphere to the path length if the sun were in the zenith." [3]
Baseline	The baseline measurement is performed in regular intervals with a calibrated reference sample in the spectrophotometer to determine the equipment's drift over time.
Degradation	loss of quality or performance; degradation can also be classified into reversible and irreversible
Diffuse	Indicates that flux propagates in all directions, as opposed to direct beam, which refers to collimated flux. [2]
Emittance	"The ratio of the radiation emitted from a surface to the radiation emitted from a blackbody at the same temperature." [4]
flux concentration	the ratio of the average radiative flux on the receiver to that incident on the mirror aperture [5]
Hemispherical	"refers to all directions above a surface" [4]
IF09	Name of the reference sample used for the executing of the Raiselife round robin campaign
Integrating sphere	"optical device to either collect flux reflected or transmitted from a sample into a hemisphere or to provide isotropic irradiation of a sample from a complete hemisphere" [2]
Irradiance	"Radiometric term for the radiant flux that is incident upon a surface" [2]
Reflectance	"The ratio of reflected [...] radiation [...] to the radiation incident upon a surface." [4]
Reproducibility	"precision under reproducibility conditions" which means "conditions where test results are obtained with the same method on identical test items in different laboratories with different operators using different equipment" [6]
Solar blind	measurement in spectral ranges in which the impact of the reflected solar flux can be neglected [7]
Solar flux	a measure of how much solar power is being radiated on a given area, commonly given in W/m ² or kW/m ² [8]
Spectral	"refers to a dependence on wavelength" [4]
Standard deviation	$stdev = \frac{\sqrt{\sum_1^n (x_i - \bar{x})^2}}{n}$ as provided with Microsoft Excel <i>STDEV.P</i>
Transmittance	"the ratio of the transmitted radiant flux to the incident radiant flux" [2]
Zeroline	The zeroline is measured once a day with no sample in the spectrophotometer to describe the noise of the sensor.
$\sigma\%$	ratio of the black body radiation value at a wavelength λ and temperature T to the integral of total black body radiation at the temperature T

1 Introduction

The global challenge of energy transition targets a more sustainable energy generation. Over the last decades, the share of renewable energies increased worldwide while Levelised Cost of Energy (LCOE) decreased. Within the last years, a further drop in LCOE, especially for photovoltaics (PV) and wind energy, made renewables cost-competitive to conventional generation technologies [9]. Large scale projects in the Middle East and North Africa (MENA) region enabled the PV price to be reduced to 29.9 \$/MWh [10]. Conventional energy sources do not show these potential for further decreases in Levelised Cost of Energy. Coal remained rather constant at 100 to 110 \$/MWh during the last decade while the LCOE of nuclear energy increased from 96 \$/MWh in 2010 to 148 \$/MWh in 2017 [9]. This enables other renewable sources with higher LCOE to become cost-competitive.

Concentrated solar power (CSP) comes along with LCOE of 98 to 181 \$/MWh in 2017 when referring to solar tower applications with storage. It is therefore cheaper than nuclear energy but still a comparatively expensive energy source [9]. However, large scale CSP projects in the MENA region offer the possibility to reduce LCOE. A new 700 MW project in Dubai aims at reducing costs to 73 \$/MWh by combining parabolic trough collectors and a solar tower with fifteen hours of storage capacity [10]. In comparison to PV, CSP plants with storage show less seasonal dependence and offer a better dispatchability of renewable energies throughout the year.

A project launched by the European Union within the Horizon 2020 programme “addresses the challenges of materials for CSP technology”. *Raiselife* “focuses on raising the lifetime” of key materials for CSP technology. This development is expected to enable a further decrease of LCOE [11]. Different working packages of this project are carried out at the joint investigation site of the *German Aerospace Centre* (Deutsches Zentrum für Luft- und Raumfahrt, DLR) and the Spanish organisation CIEMAT (*Centre of energetic, environmental and technological investigation*, Centro de Investigaciones Energéticas, Medioambientales y Tecnológicas) in Tabernas, Spain.

This thesis is part of one work package within the Raiselife project [11] that is executed at DLR/CIEMAT. It targets the spectral measurements of solar absorber coatings developed for the Raiselife programme (for more information on the programme see Appendix B). The specimens are exposed to concentrated solar irradiance at a dish facility at the DLR/CIEMAT’s investigation site in southern Spain in order to analyse their performance under realistic conditions. Thermal cycling is performed with parameters such as temperatures and solar fluxes that are supposed to occur in solar tower applications. Optical analysis is carried out regularly to evaluate possible degradation of the specimens. Optical measurements are compared with other laboratories within a round robin campaign. This bachelor thesis deals with the evaluation of the round robin campaign in order to improve the reproducibility of the optical measurements carried out at PSA (Plataforma Solar de Almería).

2 State of the art

This chapter aims at providing basic knowledge about the functional principle of concentrated solar power (CSP) and optimisation potential for this technology. Therefore, four basic technologies of CSP plants are explained in order to derive the importance of the project *Raiselife*. This leads to a description of the test bench and modifications carried out prior to this thesis.

2.1 CSP plants

Several technologies can be applied for energy generation using terrestrial solar radiation. In Germany, the most common technique is photovoltaic (PV) which directly converts the energy of incoming photons into electricity. More southern sites offer the opportunity for the installation of CSP plants that require higher direct normal solar irradiance level ($> 2000 \text{ kWh/m}^2\text{a}$) to reach the operating temperatures. Figure 1 presents an overview of the working principles of the four main concepts of power generation using CSP [12]:

Parabolic trough: Mirrors in parabolic shape with a one-axis tracking system are aligned along the axis of the trough. Incident solar radiation is focused on the absorber tube in the focal line. The receiver tube is enclosed in an evacuated glass envelope [12]. The latter is usually coated with a selective paint to guarantee a high solar absorptance and low thermal emittance. After passing the mirror field, the heat transfer fluid (HTF) is used to either create steam or directly power a turbine [13].

Solar tower: Heliostats are used to hold canted mirrors that concentrate the incident solar radiation to a central receiver on top of a tower. The number of heliostats can reach several thousands. A two-axis tracking system is required for each heliostat. Receivers are commonly made of steel tubes that are either uncoated or painted black [12]. The HTF heats the working fluid (commonly water/steam or molten salt) which powers a turbine [13].

Dish/engine systems: The mirror facets concentrate the solar radiation into the focal point of each dish. Therefore, a two-axis tracking system is necessary. In the focal point, each dish exhibits an own receiver that consists of tubes containing either a HTF or directly the working fluid for the heat engine, commonly a Stirling engine. [13]

Linear Fresnel collector: Several flat or canted mirrors concentrate solar radiation into one receiver in the focal line of the mirrors using one-axis tracking systems. Receivers may be the same ones as in parabolic troughs or contain a secondary reflector to decrease optical losses. [12]

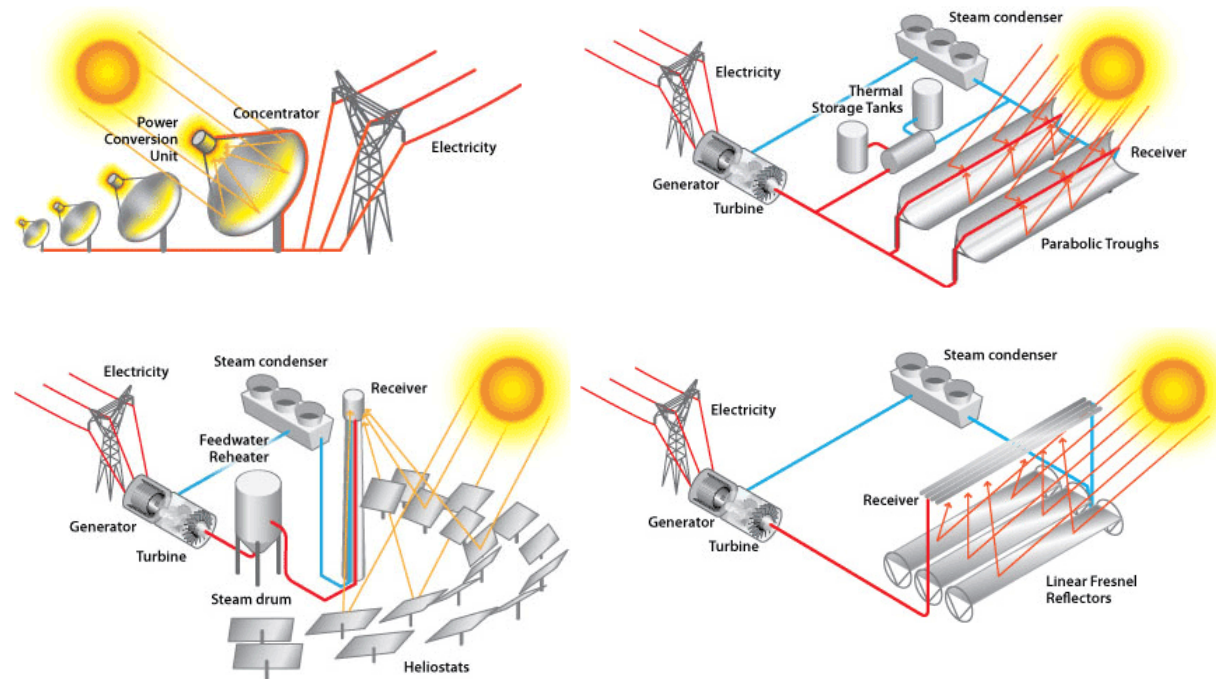


Figure 1 – Four main technologies for CSP plants [13]. Top left: dish/engine system; top right: parabolic trough; bottom left: solar tower; bottom right: linear Fresnel collector. All four concepts use mirrors to concentrate the incident solar radiation onto the receiver. Point focusing systems use a two-axis tracking system line focusing concepts use one axis to follow the course of the sun.

Concentration levels of linear focusing systems are usually below 100 while the use of central receiver systems allows high flux concentration levels of around 600 (solar tower) to above 1,000 (parabolic dish) [14]. This means, that several mirrors of a solar tower directed towards one common focal point enable higher overall efficiencies than for example parabolic troughs [15].

Within the development towards a more sustainable energy generation, natural resources need to be used more efficiently. In CSP, main influences on performance are optical losses due to low mirror reflectivity or low receiver absorptivity. Currently, mirrors can achieve over 94 % of reflectivity while receiver coatings achieve solar absorptivity above 96 %. However, degradation is a problem in CSP power plants [4]. Hence, one part of the project *Raiselife* launched by the European Union within the Horizon 2020 research programme (details see Appendix B) aims at decreasing the so-called Levelised Cost of Coating (LCOC) of solar absorber coatings.

This LCOC presents a new approach for the evaluation of solar receiver coatings and “is defined as the ratio of the total annualized coating costs (\$) to the annual thermal energy absorbed (MWh_{th})” [16].

Work package (WP) 3 within the Raiselife project aims at increasing the absorptance of thermal energy in CSP power plants. It focuses on high temperature resistant solar absorber coatings and targets an improvement in contrast to the market leader Pyromark 2500 (for details on the product see [4]). The WP contains the development of four new types of coatings provided by the project partners. These are described as:

- “a ceramic paint consisting of a primer and absorbing layer (referred as **Coating A**),
- a protective slurry aluminide coating protecting the steel substrate from hot oxidation in combination with the ceramic absorbing coating used for Coating A on top (**Coating B**),
- a solar selective magnetron-sputtered coating applied on a polished substrate (**Coating C**)
- a multi-metallic diffusion coating based on chromium and manganese applied with the powder pack cementation process (**Coating D**).” [17]

One approach for the increase of the efficiency of a coating and consequently the annual thermal energy absorbed is to increase the operating temperature, which is currently slightly above 600 °C in solar tower systems [12]. Eq. 1 [17] defines the coating's efficiency η_{coating} as a function of the solar absorptance α_s , the incident solar radiation Q_{sol} , thermal emittance ϵ_{th} and the absorber temperature T_{abs} including the Stefan-Boltzmann constant σ . The efficiency formula balances the absorbed solar radiation and the radiation emitted by the absorber. It neglects convection losses, exponent 4 making radiation dominant.

$$\eta_{\text{coating}} = \frac{\alpha_s * Q_{\text{sol}} - \epsilon_{\text{th}} * \sigma * T_{\text{abs}}^4}{Q_{\text{sol}}} \quad \text{Eq. 1}$$

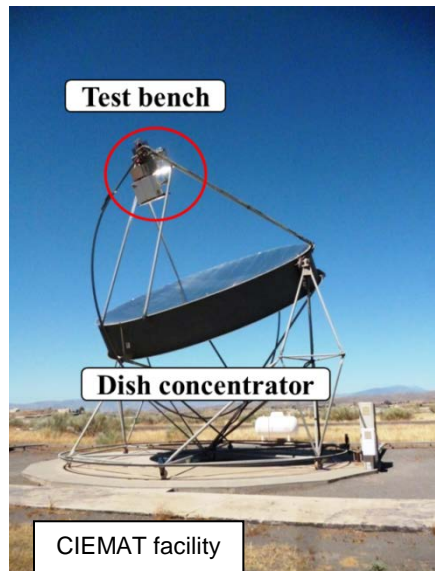
2.2 Solar cycling test bench

In order to test the performance and durability of the coatings developed within the Raiselife project, the DLR and CIEMAT have developed a unique test bench at its site at the *Plataforma Solar de Almería* (PSA) in Tabernas, Spain. It consists of a modified dish system that is used to expose the samples to concentrated solar flux. 15 tubular specimens, including three samples of each coating plus three uncoated reference samples are mounted. These tubes come along with a length of 40 mm, an outer diameter of 31.8 mm and a wall thickness of 5 mm [17].

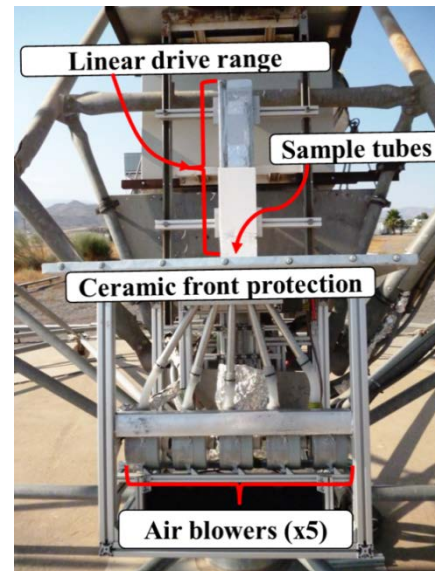
Table 1 gives an overview of the modifications of the dish test facility. Part a) shows the dish concentrator. The Stirling engine usually used for electricity generation has been replaced by the test bench shown in b). The linear drive range enables flux control on the samples as it moves perpendicular to the optical axis of the dish. A ceramic front protection is used to guarantee that the concentrated solar flux irradiates the samples only and the technical equipment is protected. Five air blowers are used to control the temperature of the samples, one for each line of the setup shown in c). Each type of coating is arranged as one string, individually cooled by an air blower. [17]

Table 1 – Overview of modifications on dish test facility [17]. a) The dish system with the test bench instead of an engine in its focus, b) the design of the test bench including a linear drive range, the sample tubes, a ceramic front protection and five air blowers, c) the view of the sample alignment showing the five rows consisting of three sample tubes each.

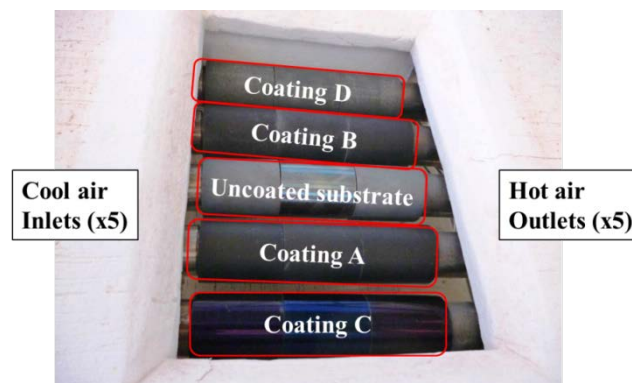
a)



b)



c)



The test procedure intends to perform an accelerated ageing test campaign by exposing the specimens to thermal cycling. It consists of three sequences illustrated in Figure 2:

- **“Heating:** All probes are first heated from 200 to 650 °C at a maximum heating rate of 30 °C/min. The average solar flux is gradually increased from 40 to 250 kW/m².
- **Dwell time:** the maximum skin temperature is then maintained at 650 °C for 30 minutes. The average solar flux is maintained at 250 kW/m² for 30 minutes.
- **Cooling:** All probes are cooled from 650 to 200 °C at a maximum cooling rate of - 30 °C/min. The average solar flux is reduced gradually from 250 to 40 kW/m².” [17]

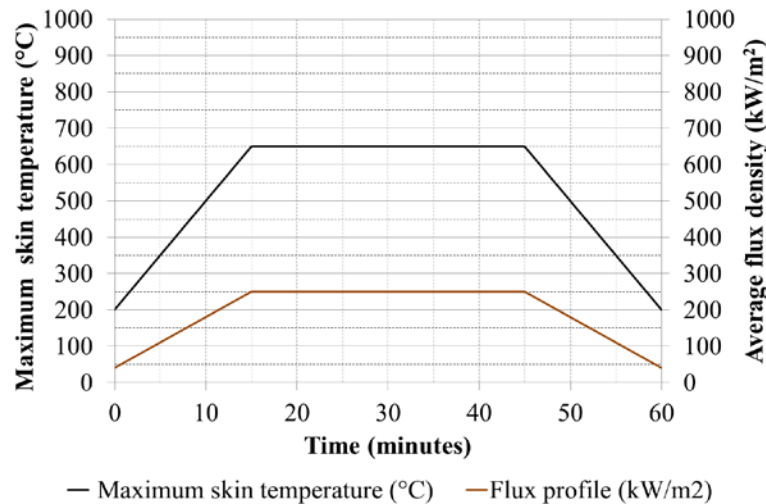


Figure 2 – Temperature and flux profile of a thermal cycle [17]. With a heating rate of 30 °C/min the specimens are heated up from a skin temperature of 200 °C to 650 °C. During a dwell time of 30 minutes, this maximum temperature is maintained constant. The cooling phase is driven symmetrically with respect to the heating phase. The development of the solar flux coincides, ranging between 40 kW/m² and 250 kW/m².

The correct measurement principle of the incident solar flux was examined in a previous master thesis. In the course of this previous thesis, the temperature measurement principle needed to be changed as the initial principle caused an overheating of the samples. The adjusted method shown in Figure 3 has improved the temperature measurement by providing more accurate values. The incident solar flux (orange) increases the skin temperature of the samples (grey) to maximum 650 °C. Each probe is equipped with one thermocouple type K (red) which is inserted in a hole drilled 1 mm underneath the surface. These temperature signals are used to the control air blowers shown in Table 1 b). Their air flow is used to cool the sample tubes from the inside to maintain the temperature according to the sequence of the cycle. The temperature setpoint for the thermocouples is calculated taking into account the substrates' thermal conductivity, as well as the coating thickness and thermal conductivity.

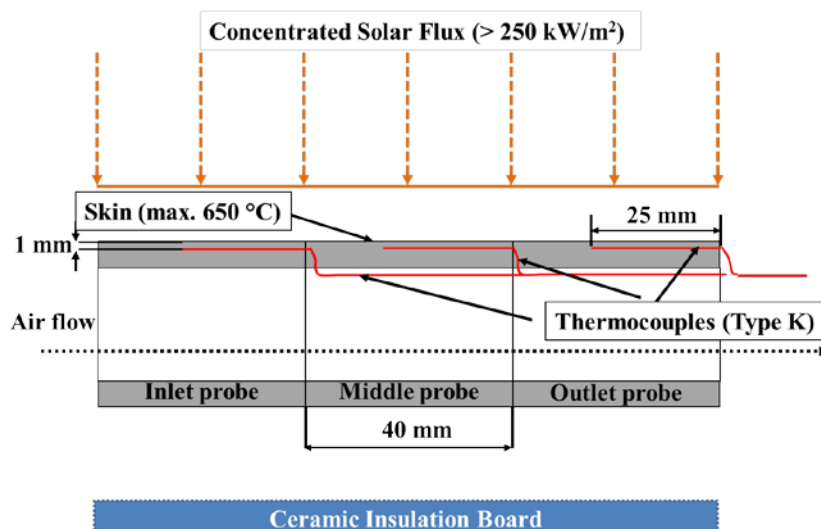


Figure 3 – Temperature measurement principle [17]. The incident solar flux increases the skin temperature of the probes to a maximum of 650 °C. An air flow within the sample tubes controls the temperature measured by the thermocouples.

Before testing and every 20 to 25 cycles, optical characterisation of the samples is carried out in the facilities of the *Optical Aging Characterization Laboratory* (OPAC) at the PSA to analyse any potential optical degradation.

A sensitivity calculation in the course of the project showed that thermal efficiency is more sensitive to changes in solar absorptance than in thermal emittance. At a solar flux of 250 kW/m² and an absorber temperature of 650 °C, “increasing solar absorptance by 1% has the same impact on thermal efficiency as reducing thermal emittance by 16.5%.” [17]

2.3 Optimisation potential

Examining the parameters of Eq. 1 as presented in Table 2 reveals the potential for the optimisation of the current method for determining thermal efficiency. The accuracy of the determination of the incident concentrated solar flux has already been investigated extensively (for more information on solar flux measurement see [18]). In the course of a prior master thesis, the temperature measurement principle has already been improved so that the samples are no longer overheated. However, the method uses calculations considering the thermal conductivity of the material and the skin temperature desired. But as the exact thickness of the different coatings is partially unknown, assumptions have been made for the calculation of the temperature gradient across the coated sample wall. The use of thermographic imaging promises the opportunity of contactless measurement of the skin temperature. If the temperature determined by a solar blind infrared (IR) camera [7] differs from the skin temperature expected in the calculations, advice for the improvement of the test procedure could be given. Nevertheless, this thesis focuses on the correct determination of the samples’ optical properties as infrared cameras require the thermal

2 State of the art

emittance of the area in question as an input parameter. Hence, the precise determination of the coatings' thermal emittance is indispensable before installing an IR camera at the dish test bench.

Table 2 – Parameters for calculating thermal efficiency and their optimisation potential. The incident solar flux and solar absorptance can already be determined accurately while temperature measurement and the determination of the thermal emittance offer potential for further optimisation.

Parameter	State of the art	Optimisation potential
σ	Stefan-Boltzmann constant (see list of physical constants)	None
Q_{sol}	Various measurement principles [18]	None
α_s	Seems verified by measurements executed by other laboratories [17], [6]	Check reproducibility
T_{abs}	Measurement principle [17] improved within prior master thesis, no overheating of the samples	Exact skin temperature unknown
ϵ_{th}	Different values determined by partner laboratories, internal mismatch	Improvement of measurement reproducibility according to ISO 22795-3

The solar absorptance values determined at PSA show only small deviations from the results of the other round robin participants while the values for the thermal emittance vary from those of the partner institutes [17]. A comparison of the measurement principles for solar absorptance and thermal emittance reveals that in the common wavelength range there is a mismatch of around 10 % as can be observed in Figure 4.

As solar absorptance values coincide with those of the round robin partners, the spectral data received from the *Lambda 1050* spectrophotometer (more details in chapter 5.1), in service for several years, seems more reliable than the data from the *Frontier FTIR* spectrophotometer, installed at OPAC in April 2017. This assumption needs to be checked before different approaches for the correction of the mismatch can be tested and evaluated.

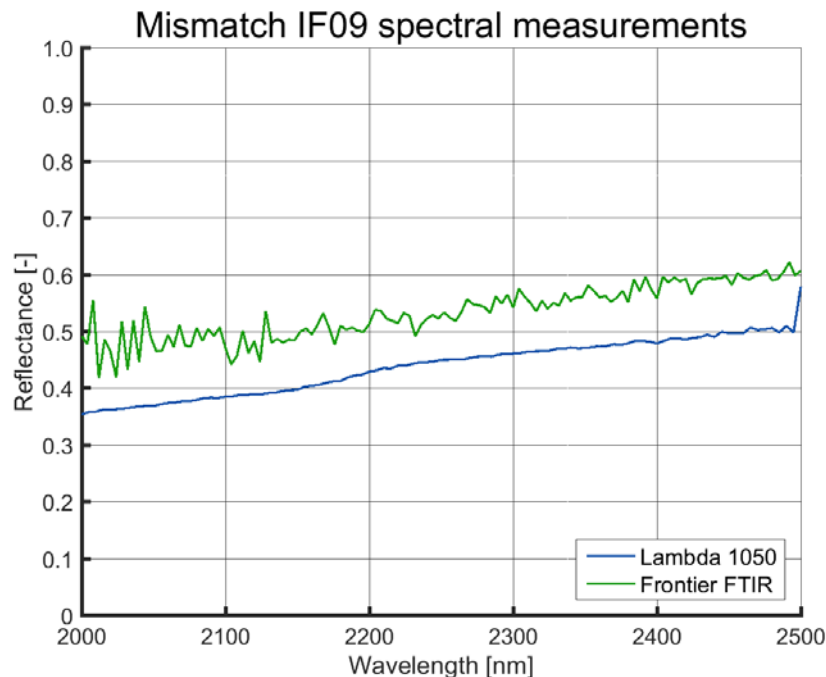


Figure 4 – Example of mismatch between spectral data of the Frontier FTIR and Lambda 1050. The Frontier FTIR spectrophotometer provides raw data with around 10 % more reflectance than the calculation results based on the measurements with the Lambda 1050. There is also more noise in the Frontier FTIR raw signal.

In order to enable the comprehension of the analysis that is to be carried out, this thesis provides background information on the relevant methods for optical characterisation with a focus on processing of data provided by two complementary spectrophotometers (chapter 3). The chapter also contains a brief description of the round robin campaign exercised for the examination of the measurement's reproducibility within the Raiselife project. After that, different approaches for the execution of common data processing of round robin measurement values are presented (chapter 4). The solar absorptance values are supposed to be proven (chapter 4.1) while approaches for the mismatch correction between the Lambda 1050 and the Frontier FTIR are the basis of the thermal emittance calculation (chapter 4.2). Results of these approaches are presented in the course of the discussion (chapter 5.3). Special emphasis is put on the internal mismatch correction (chapter 5.2.1). The corrected Frontier FTIR values are processed within the common processing of spectral data from the round robin campaign (chapters 5.2.2 to 5.2.5). Finally, the approach for the mismatch correction is compared to the round robin data (chapter 5.3.2) and a conclusion is drawn. A new measurement routine is derived (chapter 5.3.3) and the most recommendable approach for thermal emittance calculation is presented. Finally, results are summarised and an outlook for the further course of the project is presented (chapter 6).

3 Optical characterisation

This chapter provides a short introduction into optical characterisation in order to describe the expressions that will be used within the calculations in the main part of this thesis. Basic equations used in spectrophotometry as well as the equations used for the characterisation of the coatings are explained.

For the optical characterisation of a material, its interaction with radiation at different wavelengths can be used. The response differs for different materials as well as at different ranges of the electromagnetic (EM) spectrum. [19]

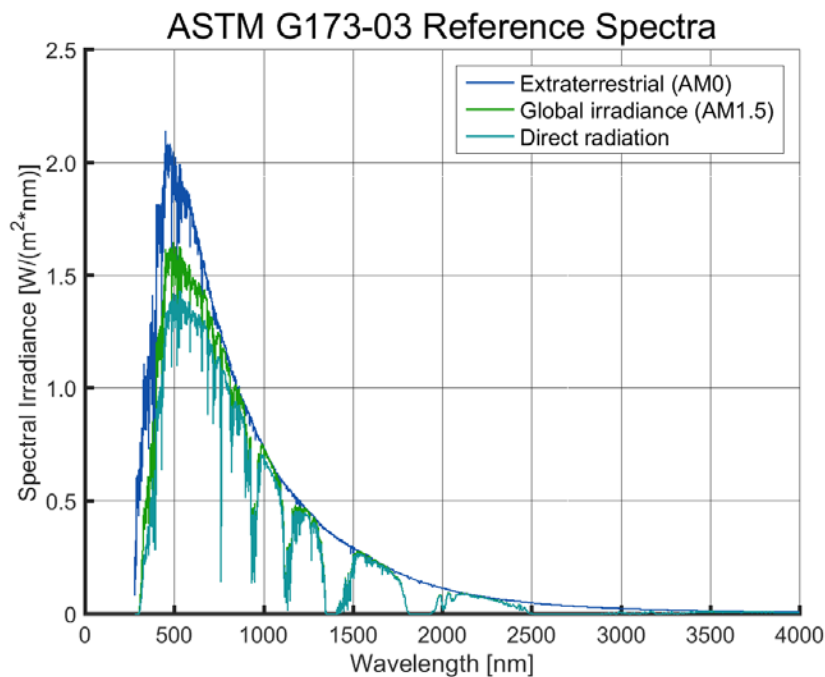


Figure 5 – ASTM G173-03 solar spectra [20]. All three curves show their maximum at around 500 W/m²nm. The main part of the direct radiation (turquoise) occurs within the visible (VIS) range. Hence, it is important that solar absorbers come along with a high absorptance within this spectral range. Global irradiance (green) also includes diffuse radiation for a tilt of 37° (AM1.5) while the extraterrestrial radiation (blue) describes the solar spectrum at top of the atmosphere and consequently comes along with AM0.

Figure 5 shows the solar spectrum according to the standard ASTM G173-03. Over 99 % of the direct irradiance occurs within EM spectra range from ultraviolet (UV) to near-infrared (NIR) at wavelengths underneath 2,500 nm. This means that it is especially important for solar absorber coatings to absorb the radiation within this range. The wavelengths of special interest for solar energy applications and therefore for this thesis include the wavelength range from around 290 nm (UV) to 25,000 nm (infrared, IR) [5].

In general, the interaction of a material with incident radiation is distinguished into three categories:

- **Absorptance α** : “the ratio of the absorbed radiant flux to the incident radiant flux.” [2]
- **Reflectance ρ** : “the ratio of reflected [...] radiation [...] to the radiation incident upon a surface.” [4]
- **Transmission τ** : “the ratio of the transmitted radiant flux to the incident radiant flux.” [2]

These three ratios enable the spectral analysis of a material, adding up to 100 % as presented in Eq. 2 [19]. All values depend on the incidence angle. This aspect is left aside from the description to provide better readability.

$$\alpha + \rho + \tau = 1 \quad \text{Eq. 2}$$

As the coating materials analysed within this project are opaque absorber tubes, the transmittance term equals zero. Consequently, measuring the reflectance is sufficient for the determination of the absorptance following Eq. 3.

$$\alpha = 1 - \rho \quad \text{Eq. 3}$$

Kirchhoff's Law of radiation states that the so-called emittance ε at a certain wavelength λ (nm) and a temperature T (K) is equal to a body's absorptance at the same wavelength and temperature as presented in Eq. 4. [19]

$$\alpha(\lambda, T) = \varepsilon(\lambda, T) \quad \text{Eq. 4}$$

This means that by knowing the coatings' reflectance of radiation at different wavelengths, the absorptance as well as the emittance can be calculated. The results are plotted over the corresponding wavelength. Degradation is likely to cause a decrease of absorptivity that results a decrease of efficiency as will be described in the course of this chapter [4]. The project Raiselife aims at the development of a solar absorber coating with high and stable absorptance values.

3.1 Spectrophotometry

Spectrophotometers are used to determine the sample's hemispherical reflectance in order to provide data for the calculation of its optical properties such as solar absorptance and thermal emittance. As the data provided from the spectrophotometers is raw data, treatment is necessary to ensure that the noise of the spectrophotometer itself does not influence the values used for the calculation. The hemispherical reflectance ρ_{hem} can be determined following Eq. 5 [21].

$$\rho_{\text{hem}}(\lambda) = \frac{\rho_{\text{hem,meas}}(\lambda) - \text{zeroline}(\lambda)}{\text{baseline}(\lambda) - \text{zeroline}(\lambda)} * \rho_{\text{hem,std}}(\lambda) \quad \text{Eq. 5}$$

The numerator is described by the difference of the measured hemispherical reflectance $\rho_{\text{hem,meas}}$ and the zeroline of the corresponding wavelength, while the denominator builds the difference

between the baseline and the zeroline. This ratio is multiplied by the hemispherical reflectance of a calibrated working standard. The latter is a reference spectrum that is supplied by the external reference laboratory OMT solutions (Netherlands).

The zeroline and the baseline are values that depend on the equipment used and need to be checked regularly. Zeroline values enable the consideration of the equipment's drift over the time. They describe the correction that is necessary to obtain reflectance values that equal 0 %.

For the spectrophotometer *Perkin Elmer UV-VIS-NIR Lambda 1050* used for the wavelength range of 280 to 2,500 nm, the procedure is well known and standardised according to DIN EN ISO 22795-3 [22]. The zeroline is measured once a day with no sample in the spectrophotometer and the lamp turned off. It describes the noise of the sensor. The baseline measurement is performed with a calibrated reference sample after every six measurements. These two factors are determined for every wavelength considered in the analysis.

For the use of the *Perkin Elmer Frontier-FTIR* for the wavelength range of 2,000 to 20,000 nm there is no experience at the PSA. Therefore, a measurement routine still needs to be defined. This is another aspect for the assumption that the values determined with the Lambda 1050 are more reliable. However, it first needs to be analysed in order to confirm this preliminary hypothesis.

3.2 Determination of optical properties

Optical properties of the solar absorber coatings in question are determined using the calculations presented in this chapter. Different measurement devices are used for different spectral ranges. To validate the data, a so-called *round robin* (details in chapter 3.3) is performed, comparing the results of the instruments used at the PSA with values obtained in other laboratories.

3.2.1 Solar absorptance

For the calculation of the solar absorptance α_s , the spectral hemispherical reflectance $\rho_{\text{hem}}(\lambda)$ is used. It is determined using the *Perkin Elmer UV-VIS-NIR Lambda 1050 spectrophotometer* and the measurement routine mentioned before. The equipment comes along with a 150 mm integrating sphere and an incidence angle of 8°. It provides data in the spectral range from 280 to 2,500 nm in steps of 5 nm [17].

As a reference to determine the solar absorptance, the solar direct normal irradiance spectrum G_{sol} at an air mass (AM) of 1.5 (as presented in Figure 5) is used as a weighting function. Knowing these parameters, the solar absorptance can be calculated with Eq. 6 [17].

$$\alpha_s = \frac{\int_{\lambda_1}^{\lambda_2} [1 - \rho_{hem}(\lambda)] * G_{sol}(\lambda) * d\lambda}{\int_{\lambda_1}^{\lambda_2} G_{sol}(\lambda) * d\lambda} \quad \text{Eq. 6}$$

It describes the proportion of solar radiation that is absorbed by the absorber and therefore represents a major contributor in the calculation of the thermal efficiency as presented in Eq. 1.

3.2.2 Thermal emittance

The spectral hemispherical reflectance $\rho_{hem}(\lambda)$ used for the calculation of the thermal emittance $\epsilon_{th}(T)$ is measured using the *Perkin Elmer Frontier-FTIR spectrophotometer* with a 76.2 mm integrated sphere that is coated with gold to enable measurements in the NIR range. The values are measured with a 12° incidence angle in the spectral range from 2,000 to 20,000 nm in steps of 4 nm. Additionally, the values in the UV-VIS-NIR range provided by the Lambda 1050 spectrophotometer are considered. [17]

While the solar absorptance is supposed to be constant at different temperatures, thermal emittance is calculated in dependence of the temperature T (K) as can be seen in Eq. 7 and Eq. 8 [17].

$$\epsilon_{th}(T) = \frac{\int_{\lambda_1}^{\lambda_3} [1 - \rho_{hem}(\lambda)] * E_{BB}(\lambda, T) * d\lambda}{\int_{\lambda_1}^{\lambda_3} E_{BB}(\lambda, T) * d\lambda} \quad \text{Eq. 7}$$

The reference value in this case is the radiant exitance of a black body E_{BB} (W/m²nm). It is determined at the same temperature and wavelength as the thermal emittance. Eq. 8 [17] shows how it is calculated according to Planck's law. The temperature T (K), the wavelength λ (nm) and physical constants such as defined in the list of physical constants are used.

$$E_{BB}(\lambda, T) = \frac{2\pi hc^2}{\lambda^5 * \left[\exp\left(\frac{hc}{\lambda kT}\right) - 1 \right]} \quad \text{Eq. 8}$$

Figure 6 shows the graphs of the ideal black body radiation for the temperature range from 300 to 800 K in steps of 100 K. According to Wien's displacement law, high temperatures shift the maximum of the black body radiation to shorter wavelengths and greater frequencies as presented in Eq. 9.

$$\lambda_{max} T = 2897.9 \mu m K \quad \text{Eq. 9}$$

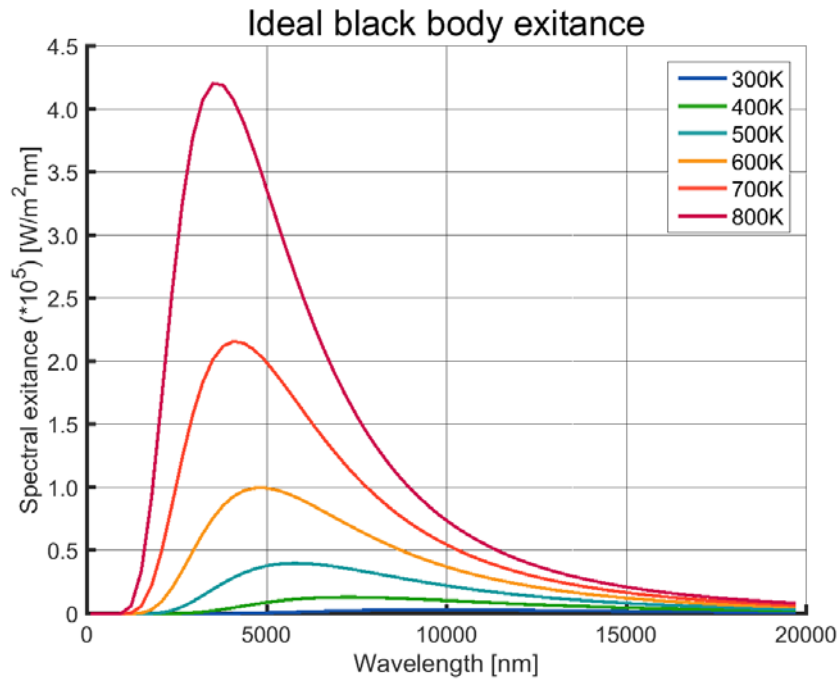


Figure 6 – Ideal black body radiation at different temperatures. The profiles depicted have been calculated according to Planck’s Law such as presented in Eq. 8. The higher the temperature, the higher the peak radiation.

The calculated thermal emittance is part of the numerator of the ratio for the determination of the thermal efficiency of solar absorber coatings as described in Eq. 1.

3.3 Round robin campaign

The round robin campaign aims at comparing optical analysis results between different laboratories participating in Raiselife project. Hence, the reference sample IF09 is measured in different laboratories to prove the reproducibility of measurements and calculations. Table 3 and Table 4 present an overview of the instruments used by different partners for the determination of solar absorptance (see chapter 3.2.1) and thermal emittance (see chapter 3.2.2). The tables show the variety of different instruments and reference samples. Not all partners are considered in the course of the round robin campaign executed within this thesis as spectral data was not provided by all participants. Only those institutes sharing their reflectance measurements are included in the calculations. These institutes are listed in the tables as CT, IE, CS and IA. DLR/CIEMAT describes the internal equipment and data at PSA.

3 Optical characterisation

Table 3 – Round robin overview for solar absorptance. The instruments used vary across the institutes. Only CT and CS use the same spectrophotometer, DLR/CIEMAT uses a new version of the same instrument. All institutes use the same integrating sphere. Four institutes use a white diffuse reference standard, only DLR/CIEMAT works with a black diffuse working standard when working with tubular absorber samples. IA uses the ASTM-E-409 AM0 reference spectrum; all other institutes use the ASTM-G173-03 AM1.5 spectrum.

Factor	CT	IE	CS	DLR/ CIEMAT	IA
Instrument	Lambda 950, Perkin Elmer	Bruker VERTEX 80	Lambda 950, Perkin Elmer	Lambda 1050, Perkin Elmer	Espectrofotómetro Cary 500
Integrating sphere	incidence angle 8° diameter: 150 mm white, diffuse				
Reference sample	White diffuse			Black diffuse	White diffuse
Reference spectrum	ASTM G173-03 (AM1.5, direct)				ASTM E-409 (AM0)
Measured wavelength range	250 to 2500 nm	320 to 2400 nm	250 to 2500 nm	280 to 2500 nm	250 to 2500 nm

Solar absorptance is commonly determined with a white diffuse integrating sphere with an incidence angle of 8° and a diameter of 150 mm (Table 3) and a white reference standard is used for the measurements in the UV-VIS-NIR range. Only the OPAC from DLR/CIEMAT uses a black diffuse working standard when measuring the solar absorptance of absorber coatings. IA works with the ASTM E-409 reference spectrum at air mass (AM) 0 while the four other institutes base their calculations on the ASTM G173-3 reference spectrum at AM1.5. The beginning of the measured wavelength ranges varies between 250 nm (CT and CS) and around 320 nm (IE) while the end wavelength is 2,500 nm in all cases.

Table 4 – Round robin overview for thermal emittance. CT and DLR/CIEMAT use the same spectrophotometer. Consequently, they use the same reference sample. In general, all institutes use gold diffuse reference standards. The incidence angle of the integrating sphere varies from 8° (IE) to 12° (CT and DLR/CIEMAT). As a reference spectrum, IA uses the black body spectrum at 300 K while the other institutes use Planck's law at 923 K.

Factor	CT	IE	CS	DLR/ CIEMAT	IA
Instrument	Frontier FT-IR, Perkin Elmer	Bruker VER-TEX 80	SOC-100 HDR, Surface Optics + Thermo-electron (Nicolet 6700)	Frontier FT-IR, Perkin Elmer	Temp2000A of AZ Technology DB-100, Gier-Dunkle
Integrating sphere	incidence angle 12° diameter: 76.2 mm Infragold, diffuse	incidence angle 8° diameter: 200 mm gold, diffuse	2 π imaging gold plated hemiellipsoid to diffuse illuminate the sample	incidence angle 12° diameter: 76.2 mm Infragold, diffuse	-
Reference sample	Gold, diffuse uncalibrated (*)	sprayed diffuse Al	gold diffuse coupon	Gold, diffuse uncalibrated (*)	Gold and diffuse standard
Reference spectrum	Planck's law for black body radiation (at 923 K)				Spectrum of the 300 K black body
Measured wavelength range	2 to 16 μm	1.5 to 16 μm	1.5 to 25 μm	2 to 16 μm	3 to 30 resp 5 to 25 μm

Reflectance in the IR range of the EM spectrum is measured with gold diffuse integrating spheres 8° (IE) or 12° (CT and DLR/CIEMAT) incidence angle (Table 4). Standards used for the measurements are commonly gold diffuse standards. IA uses the spectrum of a 300 K black body as reference spectrum and uses a portable measurement device. The other institutes calculate thermal emittance with Planck's law at 923 K (see Eq. 8). Calibrated reference standards are not yet available at DLR/CIEMAT; these are being prepared at OMT Solutions. The beginning of the measured wavelength range varies from 1,500 (IE) to 5,000 nm (IA) while the end wavelength is mostly 16,000 nm (CT, IE and DLR/CIEMAT) and 25,000 nm in the case of CS. IA names equipment with a wavelength range up to 30,000 nm.

4 Calculation methods

This chapter aims at the verification of the reflectance measurement values for all institutes participating in the Raiselife round robin campaign. Therefore, different data processing approaches are presented. They are supposed to enable a comparison of the calculated values of solar absorptance and thermal emittance in order to resolve the mismatch described in chapter 2.3 and find the reason for deviations in the values provided by the participating partner institutes. A minimisation of the standard deviation between the institutes' values promises a high measurement reproducibility.

4.1 Solar absorptance

In this section, the round robin calculations for the solar absorptance summarised in Figure 7 are presented. The aim is to compare the values provided by the partner institutes in order to prove the reliability of the values measured with the Lambda 1050 spectrophotometer.

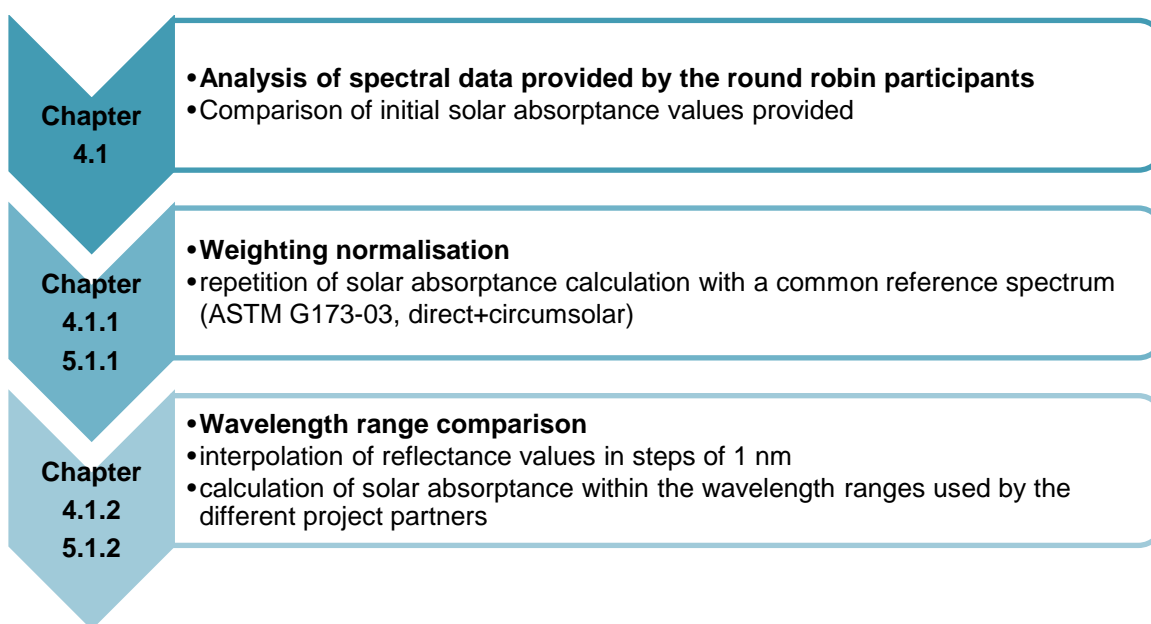


Figure 7 – Overview work steps solar absorptance. The different approaches described in the course of chapter 4.1 and discussed in chapter 5.1 are presented and explained. After the consideration of the initial values provided, the use of a common reference spectrum is guaranteed and the influence of the wavelength range is evaluated.

Table 5 presents the result values for the solar absorptance calculated by the round robin participants. No further treatment has been carried out. The values scatter around the average (avg) of 94.23 % with a standard deviation (stdev) of 0.29 %. A closer look at the specific values reveals that the highest deviations from the average are observed for IE (0.36 %) and the CT and IA (0.34 %) values. DLR and CS values show a lower deviation of 0.16 %.

Table 5 – Solar absorptance round robin values provided by the different partner institutes. The values show a standard deviation of 0.29% around the average of 94.2 %. The IA and the CT values show higher deviations.

	CT	IE	CS	DLR/ CIEMAT	IA	avg	stdev
α_s reference [%]	93.9	94.6	94.4	94.4	93.9	94.2	0.29

Figure 8 shows the spectral data used within the calculation of the values presented in Table 5. It reveals that up to a wavelength of around 1,800 nm the measured reflectance values coincide. After that, the IE and CT values exceed the values measured by DLR/CIEMAT, CS and IA. DLR/CIEMAT values show a measurement error at wavelengths around 2,500 nm. End values range from around 50 % (IA) to 58 % (DLR/CIEMAT). CT graph shows the highest measurement values with reflectances of around 56 % at 2,500 nm.

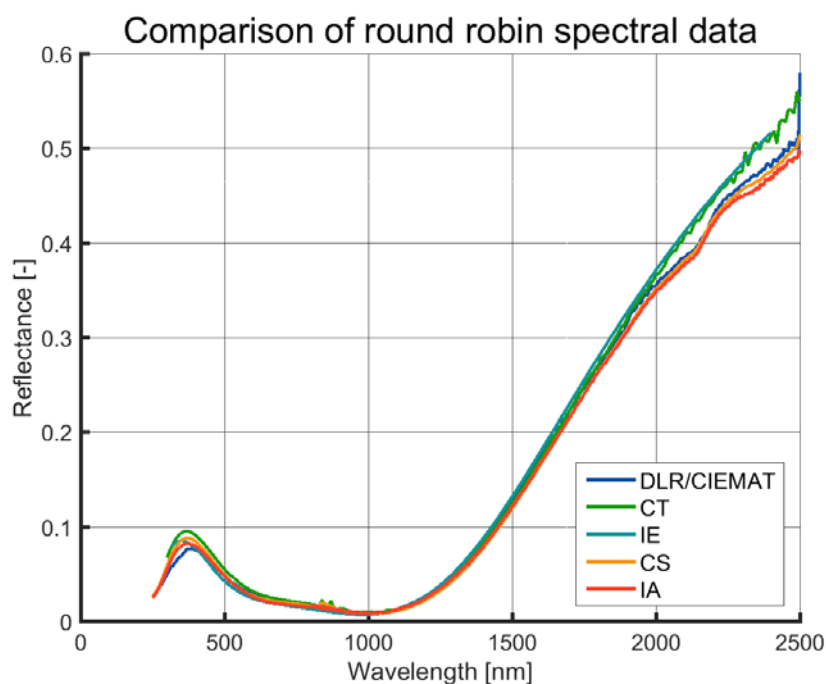


Figure 8 – UV-VIS-NIR spectral data provided by the project partners in the course of the round robin campaign. The reflectance values show deviations in the range of 1,800 nm to 2,500 nm. CT and IE data show the highest values while CS and IA data is slightly lower than DLR/CIEMAT values at higher wavelengths.

Considering the overall course of the graphs, it can be observed that the measurement values that differ the most from the mean values are those of CT, IE and IA. If the difference in measurement values leads to the difference in solar absorptance results needs to be checked by performing a common processing of data.

Figure 8 also shows that the DLR/CIEMAT measurement with the Lambda 1050 spectrophotometer coincides with the data from other institutes. Consequently, they are considered reliable and the reason for the mismatch presented in Figure 4 (see chapter 2.3) is searched in the treatment of the Frontier FTIR data.

4.1.1 Weighting normalisation

In the beginning of the round robin process, the use of one common weighting spectrum needs to be ensured. The IA value presented in Table 5 is calculated with an extra-terrestrial reference spectrum with AM 0 while all other institutes use the ASTM G173-03 reference data at AM 1.5 for direct radiation (see Table 3, chapter 3.3) [20].

All measurement datasets provided by the partner institutes are thus evaluated with the ASTM G173-03 reference spectrum to enable a comparison and to evaluate if the difference in solar absorptance values is caused by different measurement values (see Figure 8) or different calculation procedures. Results are presented in chapter 5.1.1.

4.1.2 Wavelength range comparison

Taking a look at the wavelengths used by the partners, the variations presented in Table 6 are used for the calculation of the coatings' solar absorptances.

Table 6 – Wavelength ranges of solar absorptance calculation scenarios. The different variations are derived from the intervals used by the partner institutes.

Variation	λ_{start} [nm]	λ_{end} [nm]
Var1 (CS,IA)	250	2,500
Var2 (DLR/CIEMAT)	280	2,500
Var3 (CT)	300	2,500
Var4 (IE)	~320	2,500

The wavelength range of the CT data corresponds to Var3. The actual impact of a variation in the wavelength range on the observed solar absorptance deviations is evaluated in chapter 5.1.2.

4.2 Thermal emittance

As the solar absorptance is supposed to be measured consistently, the reason for the mismatch in the overlap range of 2,000 to 2,500 nm (Figure 4, chapter 2.3) is searched in the Frontier FTIR data processing. Therefore, an approach for the mismatch correction is presented within this chapter. Furthermore, the corrected and processed Frontier FTIR data is supposed to be verified

in the course of the Raiselife round robin campaign. The approaches presented in Figure 9 provide the possibility to compare the spectral datasets used in the thermal emittance calculation.

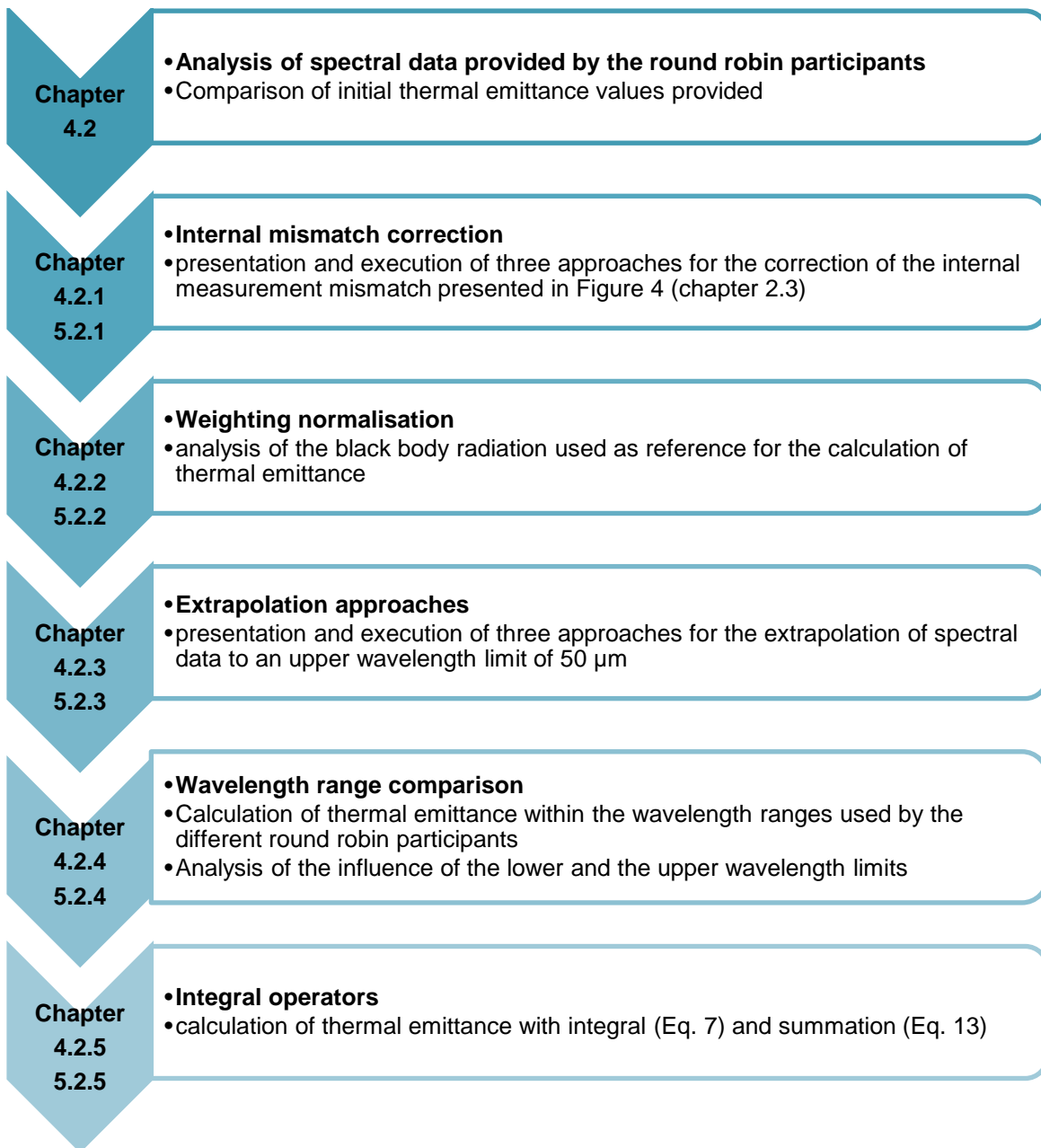


Figure 9 – Overview work steps thermal emittance. The different approaches described in the course of chapter 4.2 and discussed in chapter 5.2 are presented and explained. After the consideration of the initial values provided, the internal mismatch is corrected. After that, the use of common reference black body data is guaranteed and extrapolation is carried out with different approaches. Also, the influence of the wavelength range and the use of a summation instead of an integral equation are evaluated.

Figure 10 shows the untreated infrared (IR) measurement data as provided by the round robin participants. It reveals that the IE measurement shows noise but still coincides with the CT and CS data. The DLR/CIEMAT measurement shows high noise and exceeds the values of the part-

ner institutes. The wavelength range is cut off at 16,000 nm because of the noisy signal (see chapter 4.2.1) and the detector range. Reflectance values provided from the Frontier FTIR even exceed 100 % which proves the faultiness of the measurement values and points out the need for further processing of the data. IA's measurement data was not provided for the infrared spectral range.

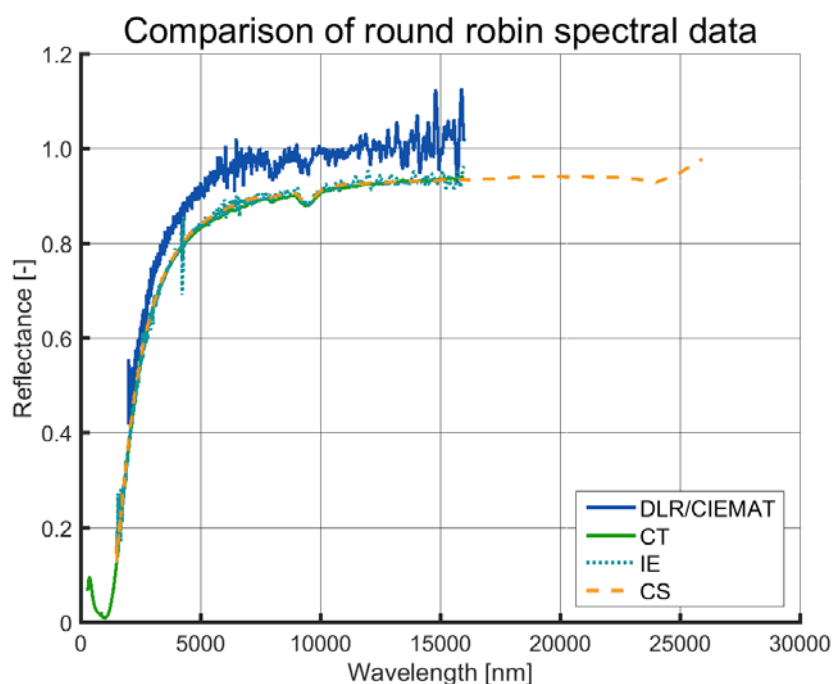


Figure 10 – IR spectral data provided by the project partners in the course of the round robin campaign. The IE signal shows noise while the CT and the CS data provide a smooth graph. However, spectra of the partner institutes coincide while DLR/CIEMAT raw data exceeds the other graphs and shows a higher noise.

Table 7 shows the result values for the thermal emittance calculated by the round robin partners. They scatter around an average of 24.9 %. The standard deviation of 0.69 % doubles the value of the solar absorptance. The IA value of 8.8 % is not considered in this calculation as it is calculated with a black body reference at 300 K (see Table 4), while all other values are reported at 923 K (650 °C). This significant deviation (16.1 %) is supposed to be caused by the temperature dependence of the thermal emittance as shown in Eq. 7.

Table 7 – Thermal emittance round robin values provided by the different partner institutes. The values show a standard deviation of 0.69 % around the average of 24.9 %. The IA value is not considered as there is no spectral data available. DLR/CIEMAT data is not considered as it needs to be corrected first.

	CT	IE	CS	DLR/CIEMAT	IA	avg	stdev
ϵ_{th} reference [%]	25.4	23.9	25.3	-	8.8	24.9	0.69

There is no thermal emittance value considered for DLR/CIEMAT because of the need for further processing of measurement data as pointed out before (Figure 10).

4.2.1 Internal mismatch correction

As the data from the Lambda 1050 spectrophotometer is considered to be reliable (see chapter 4.1), correction approaches concentrate on the Frontier FTIR measurement as shown in Figure 11. Approaches 1 and 2 target the post-processing of the Frontier FTIR IF09 raw measurement data. The third approach proposes a new measurement routine.

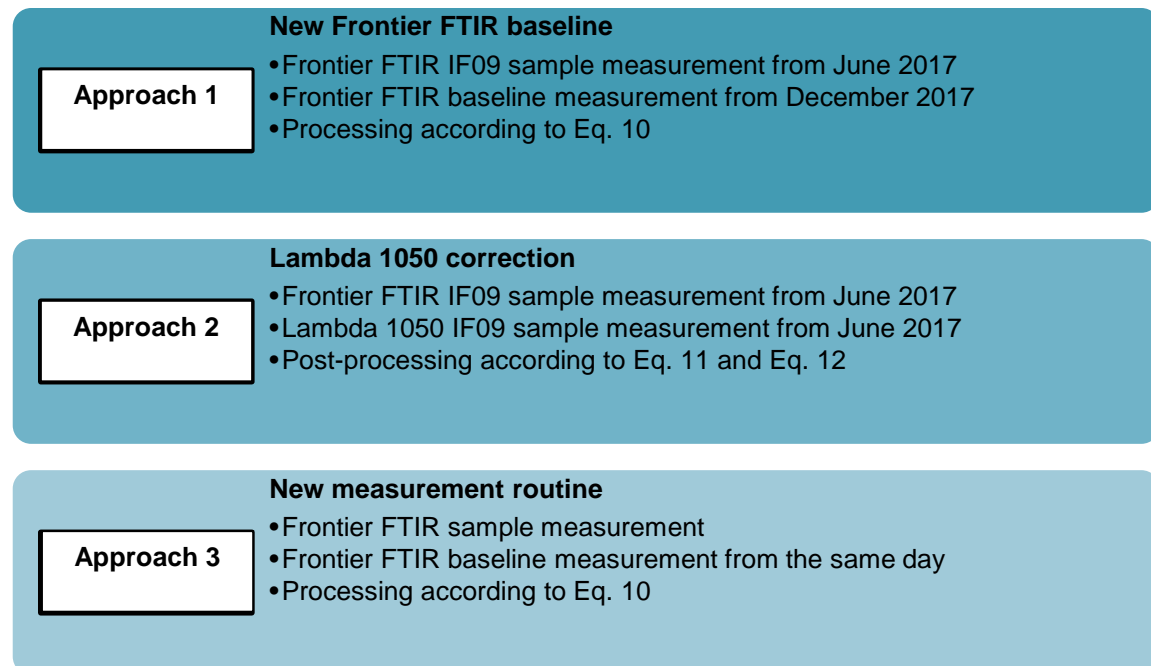


Figure 11 – Internal mismatch correction approaches. In the course of this bachelor thesis, three approaches will be executed and evaluated. Approaches 1 and 2 deal with the post-processing of the IF09 Frontier FTIR measurements while approach 3 presents a new measurement routine.

First of all, the proper functionality of the Frontier FTIR spectrophotometer is checked by measuring the integrating sphere itself. Figure 12 shows the reflectance measurement values. They are presented in the whole wavelength range from 2,000 to 20,000 nm and have been linearly interpolated in steps of 1 nm. It becomes obvious that measurement values at high wavelengths come along with high noise. Hence, the wavelength range for future analyses is cut off at 16,000 nm.

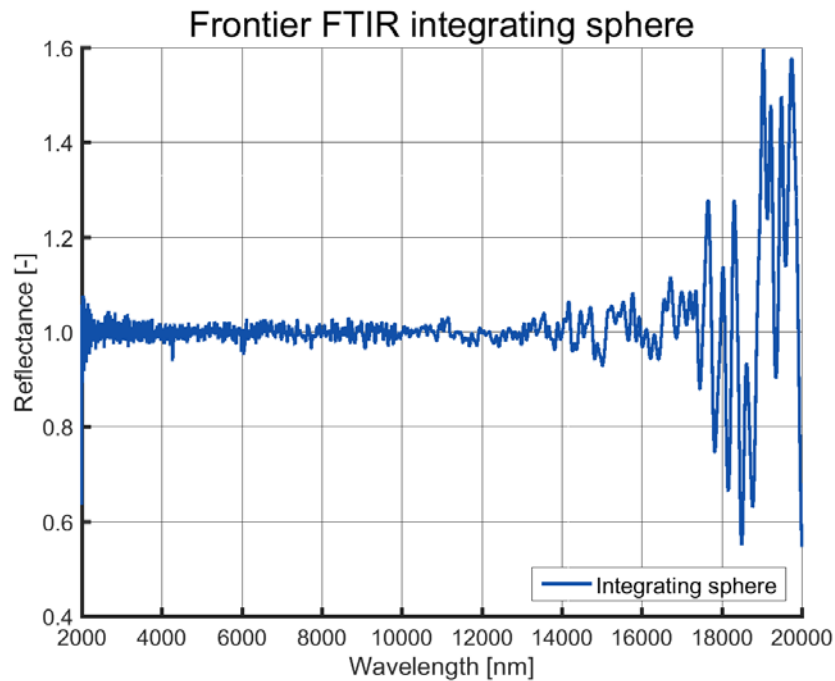


Figure 12 – Frontier FTIR integrating sphere measurement. Reflectance values depict the measurement of the integrating sphere. The signal shows high noise, especially in the wavelength range from 16,000 to 20,000 nm due to the detector. Linear interpolation in steps of 1 nm has been carried out.

For a better evaluation of measurement values, Figure 13 shows the same data reduced to the new wavelength range. Also, reflectance values are presented from 90 % to 110 %.

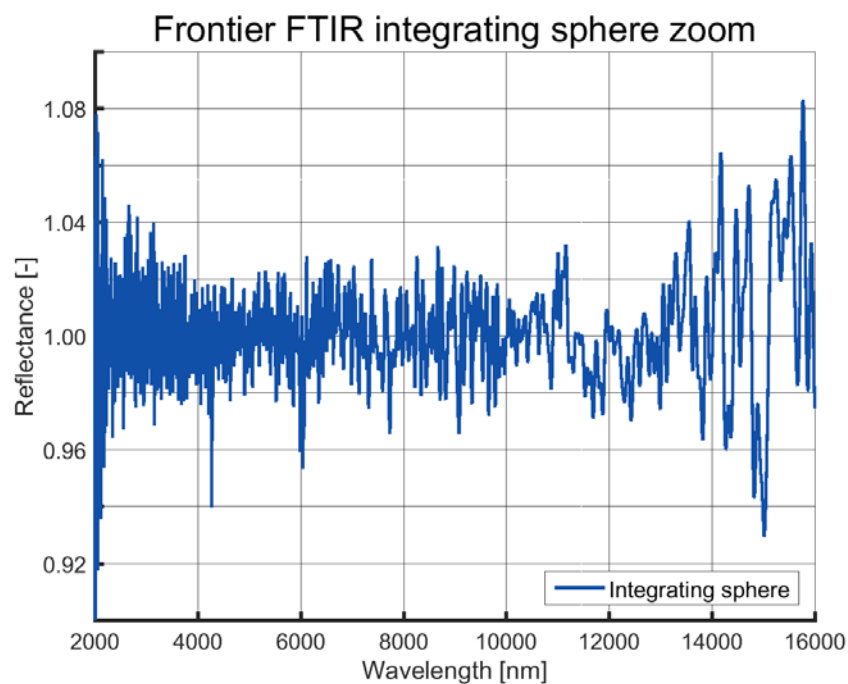


Figure 13 – Deviation of Frontier FTIR measurement zoom in. Reflectance values display measurements of the integrating sphere itself. Consequently, they depict a steady graph of 100 % but show high noise in the signal.

The measurement values scatter around 100 % which is supposed to be the integrating sphere's reflectivity. However, the signal shows high noise. Their range from approximately 90 to around 108 % can be considered the equipment's spectral sensitivity.

A closer look at the data presented in Figure 4 (chapter 2.3) reveals that the corrected Lambda 1050 data has been compared to the raw Frontier FTIR data. So, the first step for the correction of the mismatch aims at the calculations of the hemispherical reflectance values $\rho_{hem}(\lambda)$ following Eq. 5. It needs to be considered that the data provided by the Frontier FTIR spectrophotometer already represents Eq. 5 numerator because the zeroline information is not available individually. So, the Frontier FTIR data is supposed to be processed according to Eq. 10.

$$\rho_{hem}(\lambda) = \frac{\rho_{meas,FTIR}(\lambda)}{b_{meas,FTIR}(\lambda)} * \rho_{std}(\lambda) \quad \text{Eq. 10}$$

with b describing the baseline information referring to a measurement that was not taken on the measurement day but later as considered for mismatch correction approach 1 (Figure 11). It needs to be checked if processing with a post-measured baseline enables the calculation of a correct value. The result values are therefore compared to the Lambda 1050 data for the same sample. This limits the spectral range for the evaluation of the approach to the common measurement range of the two spectrophotometers from 2,000 nm to 2,500 nm. Furthermore, reference data (ρ_{std}) available for wavelengths greater than 2,500 nm is not yet available.

If the post-processing with a new baseline does not result in acceptable wavelength values, a second correction approach is worked out. Assumptions for the approach are:

- the values provided from the two spectrophotometers must be equal in the common wavelength range and
- the offset detected between the measurement values (Figure 4, chapter 2.3) is constant throughout the whole wavelength range.

They result in the calculation of the offset according to Eq. 11:

$$\rho_{offset}(\lambda) = \rho_{meas,FTIR}(\lambda) - \rho_{hem,1050}(\lambda) \quad \text{Eq. 11}$$

where the indices refer to the spectrophotometers Lambda 1050 and Frontier FTIR.

As the offset is assumed to be constant, further calculation is carried out with the average (avg) offset. Its mean value is determined in the range of 2,000 to 2,500 nm and used to extrapolate the offset following Eq. 12:

$$\rho_{hem}(\lambda) = \rho_{meas,FTIR}(\lambda) - \rho_{offset,avg} \quad \text{Eq. 12}$$

During this calculation campaign, interpolated values are used. Interpolation promises a higher resolution because Lambda 1050 measures in intervals of 5 nm while the Frontier FTIR has a spectral resolution of 4 nm.

Once the correction provides adequate results in the internal mismatch correction campaign, an evaluation of the extrapolation according to Eq. 12 needs to be exercised in the course of the round robin campaign.

4.2.2 Weighting normalisation

One important factor within the round robin campaign is the definition of universal constants. As presented in chapter 3.2.2, the black body radiation according to Planck's law requires the physical constants used in Eq. 8. During the process of data progressing within this thesis, constants are used as defined by the National Institute of Standards and Technology (NIST) [1]. Other institutes providing data for the round robin might use values that differ slightly due to rounding. Consequently, the spectral data provided needs to be processed again to ensure that the same constants and equations are used for all datasets.

First of all, a summation of all black body radiation datasets is developed in order to evaluate the share of the actual black body radiation they cover (Eq. 14, chapter 5.2.2). Besides the constants used, the resolution appears to be an important factor which is why interpolation is to be carried out in the course of the calculations presented in chapter 5.2.2.

4.2.3 Extrapolation approaches

For the determination of the thermal emittance, three approaches as presented in Figure 14 will be considered within this thesis. All approaches are executed after the interpolation of spectral data in steps of 1 nm. One round robin partner uses a different method considering the data to stay constant at a value matching the average of reflectance measures from 12,000 to 14,000 nm (approach IE). According to DIN EN ISO 22975-3 [22], the wavelength range is supposed to cover the spectrum from 2,000 to 50,000 nm. The standard proposes an extrapolation method as will be detailed in 4.2.4. The MATLAB extrapolation algorithm is based on the last 1 nm interval, using a linear algorithm.

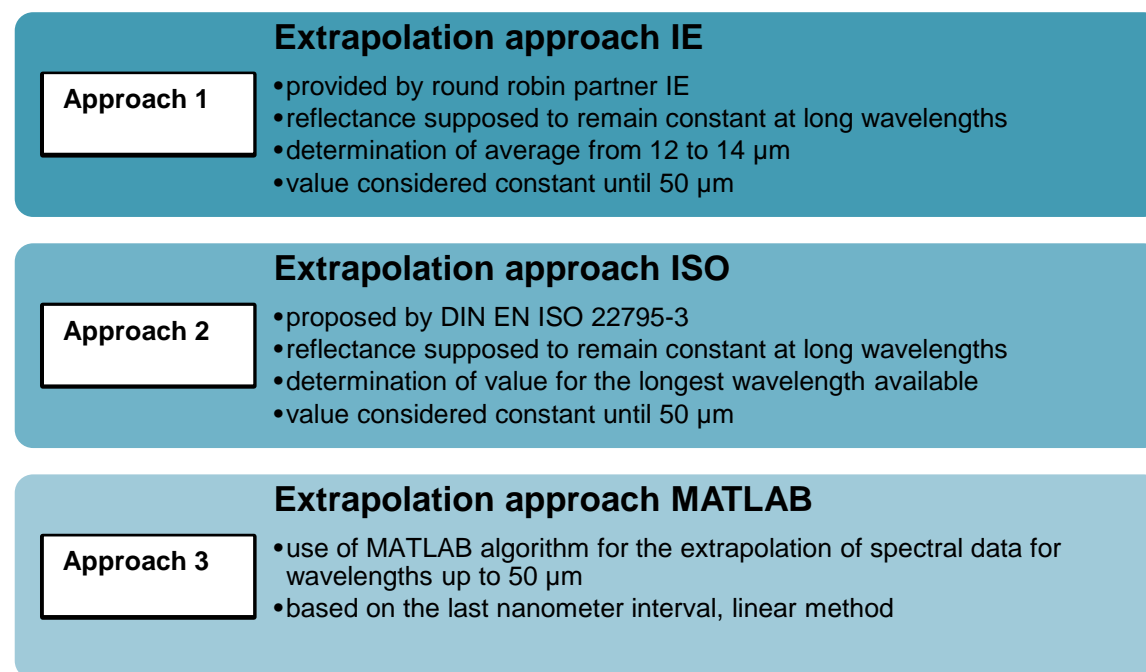


Figure 14 – Overview of extrapolation approaches. The approaches IE and ISO base on the consideration that reflectance values remain constant at long wavelengths. Approach IE expects the average reflectance between 12,000 and 14,000 nm to remain constant while the ISO approach considers the last value at the longest wavelength to remain constant. Approach 3 uses the automatic MATLAB extrapolation function.

During the calculations executed for this thesis, all methods are executed. Additionally, the MATLAB function for the extrapolation of data is used and compared to the other approaches (see chapter 5.2.3). In the end, an evaluation of these approaches is carried out.

4.2.4 Wavelength range comparison

The examination of the datasets provided by the partner institutes shows that their equipment enables measurements in different wavelength ranges or that extrapolation is executed. Starting values vary between 250 and ~320 nm while end values range from 16,000 to 50,000 nm.

Different scenarios for wavelength ranges included in the calculation are supposed to be exercised and evaluated. Table 8 presents an overview of the different wavelength ranges in question.

Table 8 – Wavelength ranges of thermal emittance calculation scenarios. The different variations are derived from the intervals used by the partner institutes. Start values range from 250 to around 320 nm while end values used are between 16,000 and 50,000 nm.

Variation	λ_{start} [nm]	λ_{end} [nm]
Var1 (DLR/CIEMAT)	280	16,000
Var2 (CS)	250	~25,000
Var3 (IE)	~320	50,000
Var4 (Frontier FTIR range)	2,000	16,000

Variations 1 to 3 represent the wavelength ranges used by at least one partner institute. Variation 4 describes the wavelength range of the Frontier FTIR measurements. Large wavelength intervals are expected to enable an increase of accuracy in the calculation of the thermal emittance, as a larger $\sigma\%$ (Eq. 15, chapter 5.2.2) is covered.

The determination of optical properties according to DIN EN ISO 22975-3 requires the consideration of the thermal emittance in a spectral range from 2,000 to 50,000 nm. It proposes an extrapolation from 25,000 nm to 50,000 nm, assuming the reflectance to remain constant in this range.

4.2.5 Integral operators

Another approach that needs to be included in the processing of data is the equation used for the calculation of the thermal emittance itself. Chapter 3.2.2 of this thesis presents an equation using integral calculation while DIN EN ISO 22975-3 proposes the calculation using Eq. 13.

$$\varepsilon_{th}(T) = \frac{\sum_{\lambda_1}^{\lambda_3} [1 - \rho_{hem}(\lambda)] * E_{BB}(\lambda, T) * d\lambda}{\sum_{\lambda_1}^{\lambda_3} E_{BB}(\lambda, T) * d\lambda} \quad \text{Eq. 13}$$

Different integration and summation methods provided by MATLAB are tested in order to determine whether they lead to a variation in thermal emittance values.

5 Results and discussion

During this chapter, the results of the calculation approaches presented in chapter 4 are shown and discussed. Possible reasons for deviations are given.

5.1 Solar absorptance

The comparison of the spectral data in the UV-VIS-NIR range used for the calculation of the solar absorptance with a common reference spectrum is executed via Microsoft Excel. The interpolation and calculation within a common wavelength range is executed with MATLAB.

5.1.1 Weighting normalisation

For the weighting, all datasets are evaluated following Eq. 6 using the ASTM G173-03 reference spectrum. Table 9 presents an overview of the solar absorptance values determined during the weighting process and compares them to the values provided by the round robin partner institutes presented before (see chapter 4.1). The wavelength intervals are used as by the partner institutes in order to examine the influence of the ASTM G173-03 reference spectrum only. As ASTM G173-03 spectral data is available for wavelengths greater than 280 nm only, IA and CS data is cut and values from 250 to 280 nm are neglected.

Table 9 – Comparison of weighted solar absorptances with reference values. Values determined within the verification process mainly coincide with the reference values named by the partner institutes, the IA value differs. The standard deviation of the weighted values rose from 0.29 % before to 0.36 % after processing.

	CT	IE	CS	DLR/ CIEMAT	IA	avg
Before processing [%]	93.9	94.6	94.35	94.43	93.90	94.24
Weighting normalisation[%]	93.90	94.55	94.35	94.43	95.03	94.45
Δ [%]	0.0	0.05	0.0	0.0	-1.13	

The weighting shows that the values calculated by institutes using the ASTM G173-03 direct reference spectrum at AM1.5 coincide with the values determined in the course of the verification process. Only the initial solar absorptance calculated from IA using AM0 differs around 1 %.

Evaluating the different measurements, the average of weighted solar absorptances is determined to be 94.24 % with a standard deviation of 0.36 %. This means that the use of a common ASTM G173-03 reference spectrum leads to a slight increase of standard deviation due to the comparatively high IA value. However, no value deviates more than ~0.5 % from the mean solar absorptance.

5.1.2 Wavelength range comparison

After increasing the standard deviation by the use of a common reference spectrum, the solar absorptance calculation is to be executed with a common wavelength range for all datasets. The variations considered for the scenarios are presented in Table 6 (chapter 4.1.2). All scenarios have the common end wavelength of 2,500 nm while start values range from 250 to around 320 nm. Table 10 shows the results for the calculation with a common wavelength range. Interpolation in steps of 1 nm has been carried out.

Table 10 – Variation of the wavelength range for solar absorptance. All values have been calculated with an end wavelength of 2,500 nm while the start wavelength (λ_{start}) is varied in order to perform the three variations used by the round robin partners. Reflectance values have been linearly interpolated in steps of 1 nm. Changing the start wavelength has no effect on the solar absorptance value which is why only one scenario is depicted.

λ_{start} [nm]	CT [%]	IE [%]	CS [%]	DLR/ CIEMAT [%]	IA [%]
280	93.95	94.45	94.40	94.44	94.51

The variation of the start wavelength from 250 to 320 nm shows no deviation in solar absorptance. The reason for that is similar to the reason presented for the thermal emittance in Figure 24 (chapter 5.2.4) as the ASTM G173-03 solar reference spectrum (Figure 5, chapter 3) shows only slight increases at small wavelengths.

Solar absorptance now ranges between 93.95 % (CT) and 94.51 % (IA). The mean solar absorptance is 94.35 % and the standard deviation is 0.20 %. After processing, the IA value is the only one showing more than 0.5 % deviation from the initial value. This is explained with the use of the reference spectrum at AM1.5. The value's deviation from the mean has been reduced to 0.16 % instead of 0.58 %. CT's deviation of 0.40 % can be explained by smaller reflectance values (Figure 8, chapter 4.1). Small values for $\rho_{\text{hem}}(\lambda)$ lead to a greater numerator in Eq. 6 and consequently result in greater values for solar absorptance.

5.1.3 Summary

Figure 15 shows the recalculation of solar absorptance values in the course of the Raiselife round robin campaign at PSA. Results are presented for each institute and as average for the different approaches (chapters 5.1.1 and 5.1.2) executed within this thesis. Standard deviations are included as error bars.

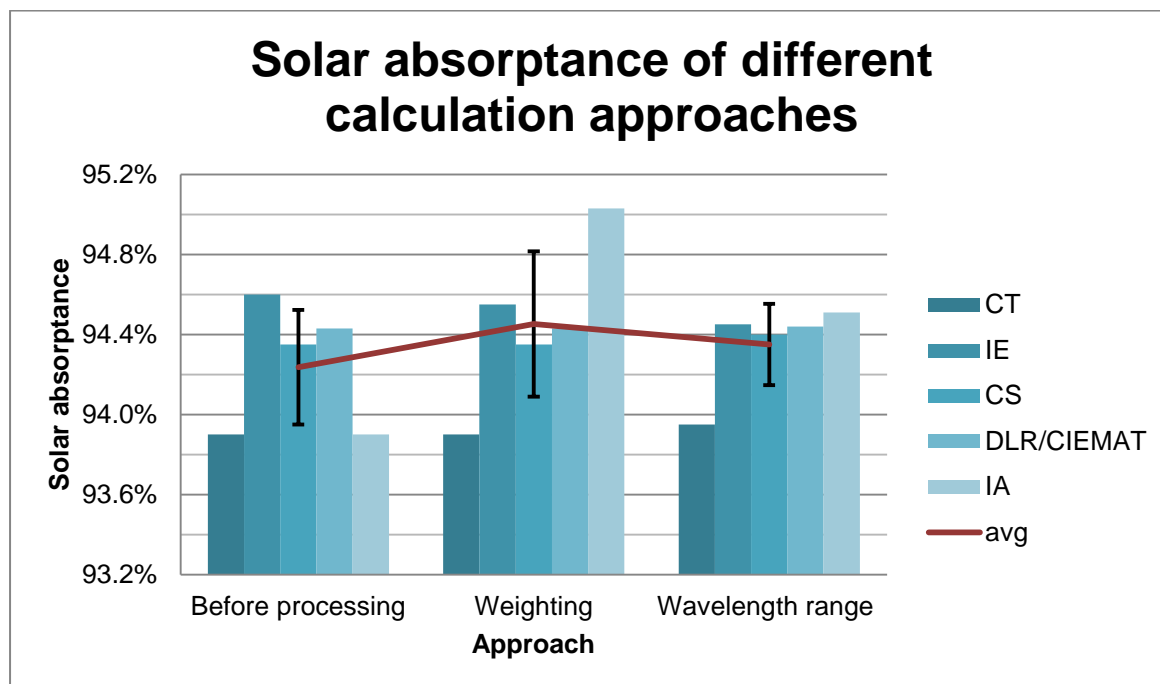


Figure 15 – Overview: solar absorptance calculation approaches and their results. For each approach, the calculation results as well as the average (avg) and standard deviation (stdev, presented as error bars) are considered. The weighting with a common reference spectrum leads to a rise in stdev from 0.29 to 0.36 %. Processing data with the same wavelength range enables a decrease of stdev to 0.20 %.

Using the ASTM G173-03 direct reference spectrum as a common basis (weighting) leads to a rise in standard deviation from 0.29 % to 0.36 % as the IA value increases. But the interpolation of reflectance values and the use of a common wavelength range enable the reduction of the standard deviation to 0.20 %. The variation of the start wavelength does not affect the result significantly (see Table 10, chapter 5.1.2). After processing, the IA value approaches towards the average. Small standard deviations are observed for solar absorptance values, which can be interpreted as high reproducibility within the participants of the Raiselife round robin campaign.

The deviations of the initial values and solar absorptance results after processing (wavelength range) range from 0.00 % (CS) to 0.61 % (IA, due to the initial use of ASTM E-409 at AM0). The average value rises from 94.24 % to 94.35 %.

Figure 16 shows the flow chart of the processing steps that have been implemented in the course of this thesis. All data sets have been linearly interpolated in steps of 1 nm. The wavelength range of consideration starts at 280 nm and ends at the equipment's limits of 2,500 nm. Solar absorptance calculation is carried out according to Eq. 6 (chapter 3.2.1) with the common reference spectrum of direct radiation at AM1.5 as defined by the ASTM G173-03 standard.

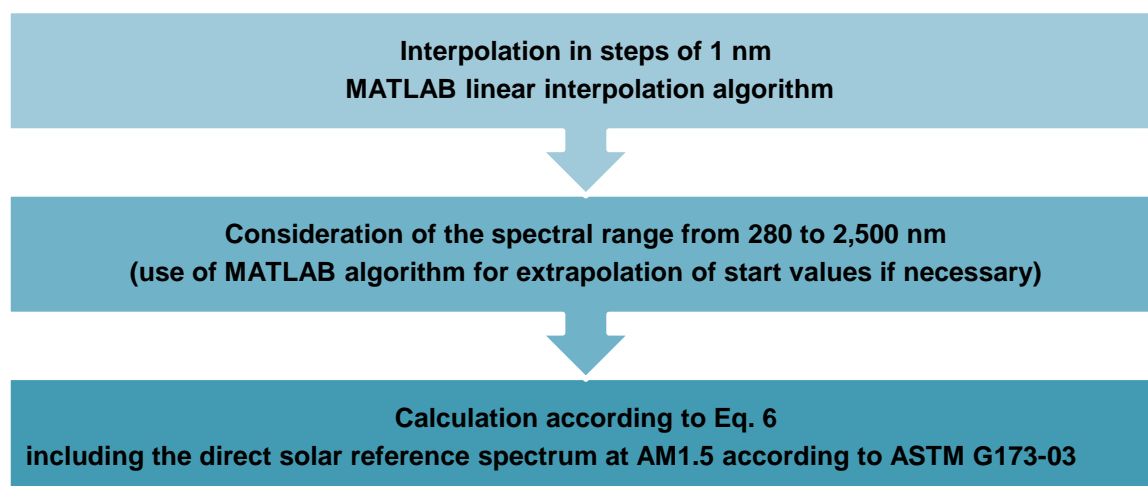


Figure 16 – Flow chart of solar absorptance data processing within the Raiselife round robin campaign. All values have been linearly interpolated in steps of 1 nm in the spectral range of 280 to 2,500 nm before calculating solar absorptance according to Eq. 6 with the ASTM G173-03 reference spectrum for direct solar radiation.

5.2 Thermal emittance

The calculations steps considered during the evaluation of thermal emittance values are implemented using different MATLAB scripts that have been developed in the course of this thesis.

5.2.1 Internal mismatch correction

First of all, the Frontier FTIR raw data is processed with new baseline data as described in chapter 4.2.1. Therefore, the IF09 round robin measurement values from June 2017 are post-processed with a baseline taken in December 2017. For a first evaluation of the approach, the result is shown in Figure 17. The processed Frontier FTIR data (Frontier FTIR calc, blue) results in reflectance values below 5 % while the Lambda 1050 values (green) increases linearly from 9 % to 16 % and the Frontier FTIR raw signal (turquoise) ranges from 20 % to around 26 %.

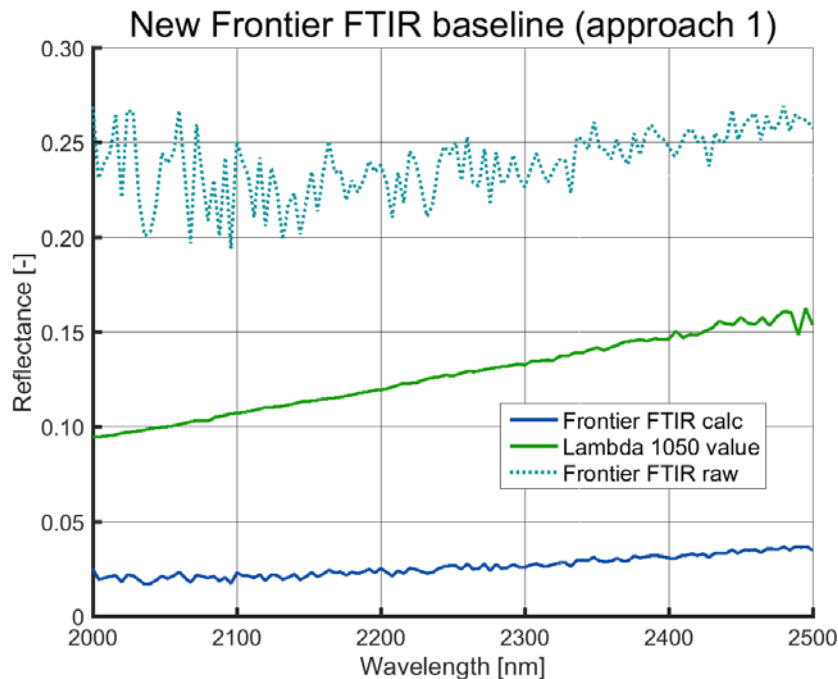


Figure 17 – Post-processing approach 1 for Frontier FTIR data. The use of baseline data that is not from the same day as the measurements points out the importance of this fact. Noise in the raw signal is reduced, but the new values are not suitable for the calculation of the thermal emittance as they vary strongly from the Lambda 1050 data.

This deviation between the Lambda 1050 value and the calculated Frontier FTIR value show the necessity of a baseline measurement from the same day as the measurement itself. As this is not available in case of the IF09 spectral data, the second approach for the postprocessing of data (see chapter 4.2.1) is executed. Figure 18 shows the result values for the Frontier FTIR values treated with the second approach and compares them to the Lambda 1050 data in the common wavelength range from 2,000 to 2,500 nm.

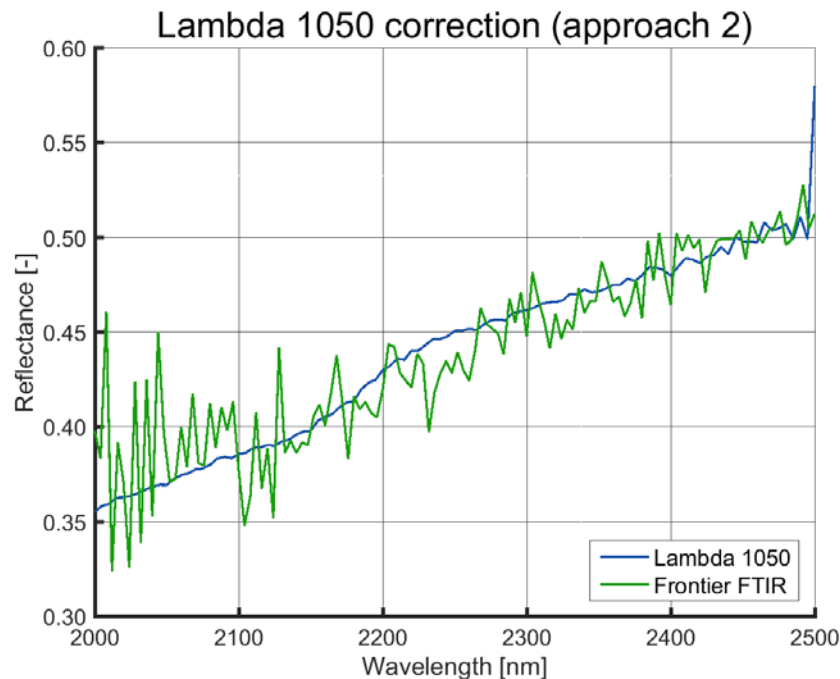


Figure 18 – Post-processing approach 2 for Frontier FTIR data. The calculation approach enables the approximation of the Frontier FTIR measurement values to the Lambda 1050 values. This approach promises the possibility of a post correction of the raw Frontier FTIR data collected within the Raiselife project.

This approach enables an approximation of the Frontier FTIR values (green) to the Lambda 1050 reflectance measurements (blue) although the graph still shows noise.

As the internal comparison results in a promising approach for the mismatch correction, it is applied to the full wavelength range according to Eq. 12. Figure 19 shows a comparison of the Frontier FTIR values corrected according to approach 2 and the round robin values as presented in 4.2. The corrected DLR/CIEMAT spectral data now approaches the reflectance measurement values provided by CT, IE and CS although it still shows high noise and the DLR/CIEMAT reflectance values are slightly smaller. The additional use of a MATLAB smooth function seems promising in order to minimise this noise (more details see Appendix D). However, the comparison shows that the extrapolation approach of the mismatch correction according Eq. 12 already enables an approximation to the other institute's data. These datasets shown in Figure 19 represent the values used for the calculations in the further course of this thesis.

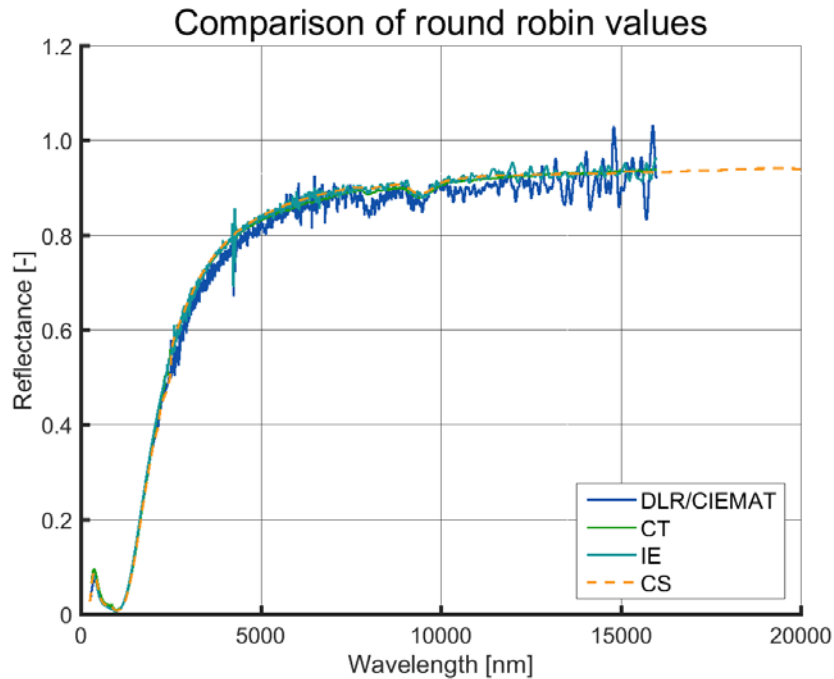


Figure 19 – IR spectral data used within the round robin campaign. The partner institute's data is presented as provided by the institutes while the Frontier FTIR data has been post-processed. The signal shows high noise, but the general trend shows an approximation to the other data. Hence, the correction approach is considered as a base for a new calculation of thermal emittance.

The conclusion previously derived from Figure 17 enables the finding of a new measurement routine for the processing of reflectance measurements with a baseline measured the same day as described in approach 3 in Figure 11 (chapter 4.2.1). Figure 20 shows the spectral data of a black diffuse working standard (WS) used at the OPAC facilities at PSA. The OPAC data (blue) is taken as reference data in order to evaluate the result values. Consequently, the wavelength range is limited to 2,000 to 2,500 nm due to the common wavelength range of the spectrophotometers.

Figure 20 reveals that mismatch correction approach 3 with a baseline from the same day (green) enables a better approximation to the Lambda 1050 data. The Frontier FTIR graph shows noise, but generally coincides with the Lambda 1050 measurement data. In order to perform a more detailed evaluation of this new measurement process, the deviations between the data of the two spectrophotometers and their standard deviations are analysed (details presented in Figure 35, Appendix C). Resolutions of 20 nm (no interpolation performed) and 1 nm (linear interpolation performed) are considered. The standard deviation between the two graphs is reduced from 4.4 % (20 nm resolution) to 1.6 % (1 nm resolution).

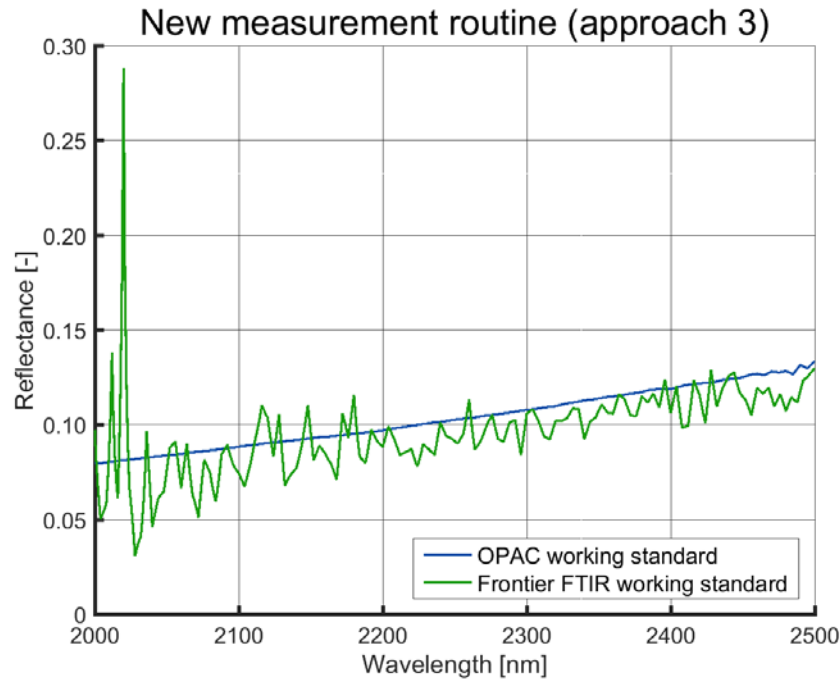


Figure 20 – Comparison of WS measurements with new measurement routine. Frontier FTIR values have been corrected with a baseline that was taken the same day as the sample measurements. The sample in question is the black diffuse working standard used in the OPAC for measurements of the baseline.

This first analysis proves the calculation method according to Eq. 10 for the interval between 2,000 and 2,500 nm. A further evaluation cannot be carried out as a reference standard for wavelengths beyond 2,500 nm is not yet available at PSA (see chapter 4.2.1).

5.2.2 Weighting normalisation

To compare the different values used for the black body radiation, the datasets provided by the round robin partner institutes are evaluated. Therefore, they are compared to the integral of the exitance of an ideal black body $E_{BB,ideal}$ (W/m^2) which can be calculated using Eq. 14 [5].

$$E_{BB,ideal} = \int_0^{\infty} E_{BB}(\lambda, T) = \sigma * T^4 \quad \text{Eq. 14}$$

with σ being the Stefan-Boltzmann constant and T the temperature of the black body in question. It is 923 K (650 °C) in this case. This value is then used to normalise the black body radiation data provided by the round robin participants or calculated according to Eq. 8 at DLR/CIEMAT respectively. Eq. 15 presents the calculation used for the evaluation of black body exitance weighting.

$$\sigma \% (\lambda) = \frac{\sum_{\lambda_1}^{\lambda_2} E_{BB,institute} (\lambda, T)}{E_{BB,ideal} (T)} \quad \text{Eq. 15}$$

Figure 21 shows the values derived. They represent the ratio of the black body radiation value at a wavelength λ (nm) and temperature T (923 K) to the integral of total black body radiation at the same temperature. It enables an evaluation regarding the percentage of total black body radiation at 923 K covered by the datasets used as denominator in Eq. 15.

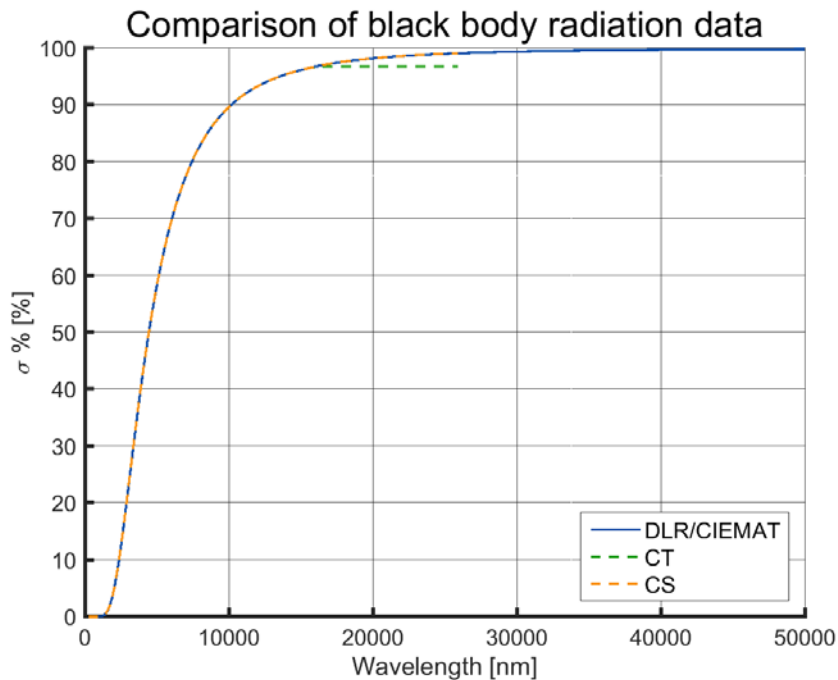


Figure 21 – Comparison of black body reference data at 923 K. It reveals that all datasets provided by the round robin partners cover the maximum of black body radiation. CS data equals DLR/CIEMAT data; CT values remain constant at wavelengths over 16,000 nm.

As can be seen in Figure 21, all $\sigma\%$ curves add up to almost 100 % of the ideal black body existence. CT values are available to wavelengths up to 16,000 nm only. Final values range from 96.77 % (CT) to 99.9 % (DLR/CIEMAT). The round robin partner IE is not considered in this analysis as no black body reference data has been provided in the course of the round robin campaign.

In order to eliminate errors due to small deviations, the thermal emittance calculation is executed with the DLR/CIEMAT black body radiation data at 923 K calculated as presented in Eq. 8 (see chapter 3.2.2).

5.2.3 Extrapolation approaches

For the proper evaluation of the coatings, the wavelength range considered in the calculation needs to be adapted. Therefore, extrapolation is necessary. The different approaches presented in the course of chapter 4.2 are to be implemented and evaluated.

Figure 22 shows the comparison of the raw spectral data from CT and the three different extrapolation approaches. The raw data is plotted before interpolation (blue) while the processed data has been interpolated in a resolution of 1 nm. As a means of comparison, CS spectral measurement is included (red). The institute provides measurements up to a wavelength of 25,000 nm and is used for the evaluation of the extrapolation approaches.

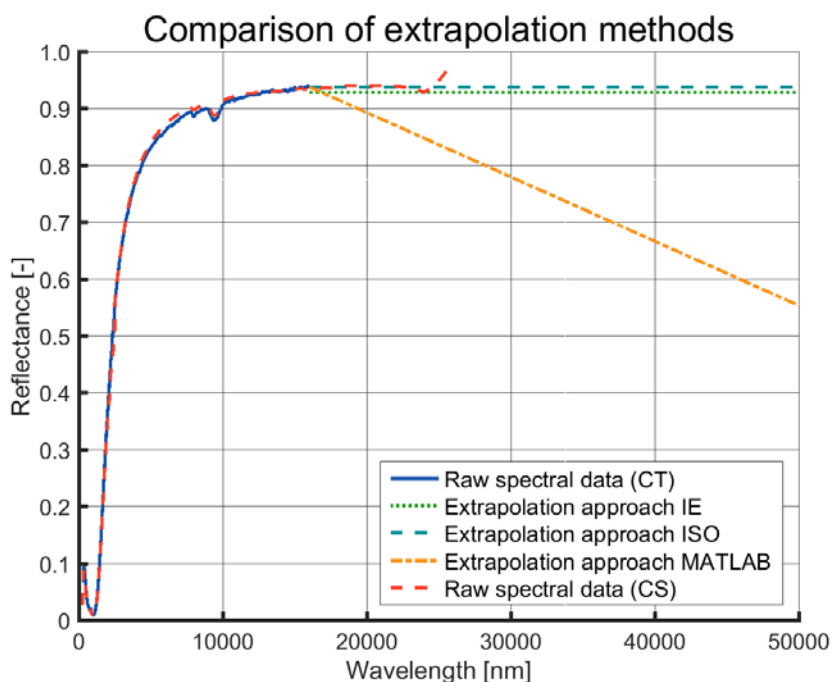


Figure 22 – Comparison of extrapolation methods. The values calculated with the IE extrapolation method are slightly lower than those calculated according to DIN EN ISO 22975-3. CS reference data verifies the extrapolations and rather coincides with the ISO approach. The MATLAB linear extrapolation method is based on the last 1 nm and does not provide satisfactory results.

CT extrapolation values following DIN EN ISO 22975-3 slightly exceed IE values (green). In the wavelength range considered in Figure 22, both approaches provide constant data beyond 16,000 nm. The ISO end value (turquoise) is 93.91 % while the final IE value is 92.94 %, which is 0.97 % lower. CS reference values coincide with the ISO extrapolation values in the range from 16,000 to 25,000 nm. The extrapolation approaches according to IE and ISO are confirmed by the CS measurement data.

The extrapolation approach generated by MATLAB (orange) shows linear decreasing values. This course of the graph can be excluded because selective absorber tubes are known to show constant reflectance values at great wavelengths while the MATLAB extrapolation algorithm considers the last interval and derives a linear trend. Hence, the MATLAB extrapolation function will not be considered in the further course of this analysis. However, the CS graph shows a drift at the end of the dataset due to a variable wavelength resolution.

Figure 23 shows a comparison of the extrapolation approaches ISO and IE and thermal emittance results derived from these values for a temperature of 923 K. Deviations are indicated as Δ . The maximum difference is 0.11 % (IE data).

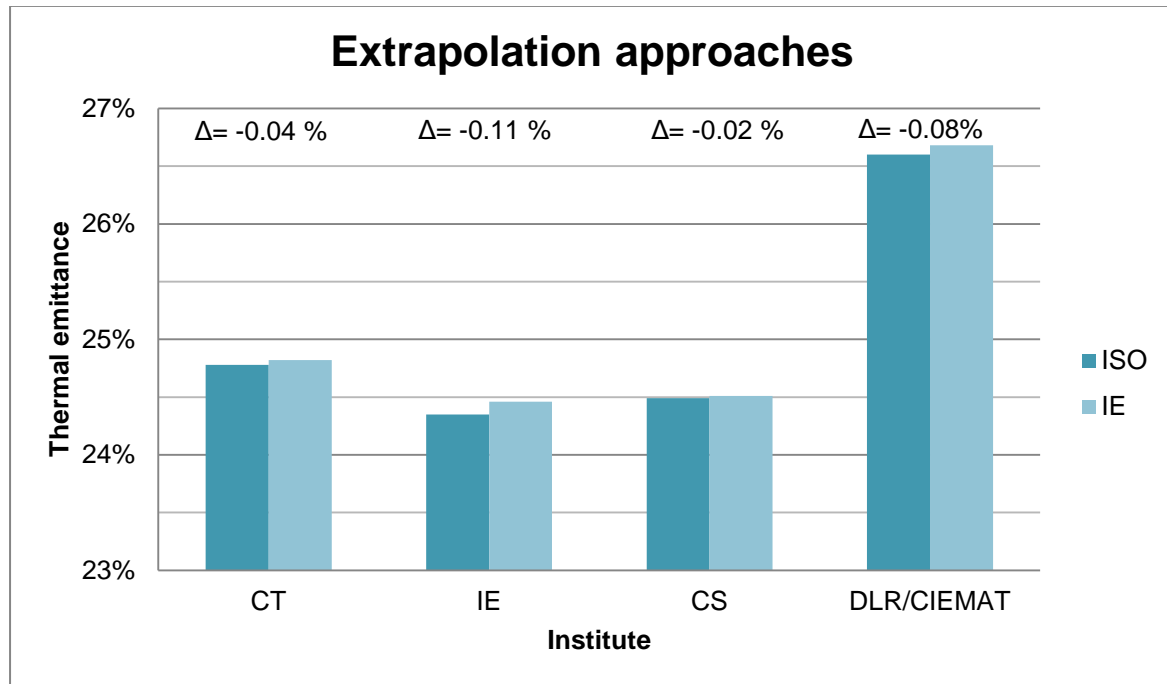


Figure 23 – Absolute comparison of extrapolation approaches. Both approaches are considered at 923 K and in the highest resolution, which is the wavelength range from 280 to 50,000 nm. The results range around 24.5 %, only the post-processed DLR/CIEMAT value exceeds 26.5 %.

As a means to evaluate the two approaches in question, the results are compared to the initial thermal emittance values provided by the other institutes within the round robin campaign. The results are shown in Table 11. ISO values are compared to initial round robin values. There are no DLR/CIEMAT values included in this campaign as former thermal emittance had been calculated with the Frontier FTIR raw data.

Table 11 – Relative comparison of ISO extrapolation approach. The approach is compared to the datasets provided by the round robin partners. All values refer to 923 K and match the comparison data with less than 1 % deviation. For DLR/CIEMAT data, no comparison is executed because round robin data refers to unprocessed data. ISO extrapolation values are subtracted from initial values.

	λ_{start} [nm]	λ_{end} [nm]	CT [%]	IE [%]	CS [%]
Initial values	Variable as used by the institute		25.4	23.9	25.3
Δ ISO	280	50,000	0.62	-0.45	0.81

No deviation exceeds 0.81 % (CS) and in general the thermal emittance values basing on the DIN EN ISO 22975-3 extrapolation are slightly smaller than those basing on the IE approach. The ISO approach results in higher reflectance values and high values of $\rho_{\text{hem}}(\lambda)$ in Eq. 7 or Eq. 13 respec-

tively lead to smaller numerators and hence result in smaller thermal emittance values. As the deviation of the results is within a range of around ± 0.1 % (Figure 23), both approaches are considered applicable.

5.2.4 Wavelength range comparison

For the analysis of different wavelength ranges and their influence on thermal emittance, the calculation according to Eq. 7 needs to be carried out using the different start and end values presented in Table 8 (see chapter 4.2.4).

Table 12 shows thermal emittances calculated with variation in the lower wavelength limit of 280 nm. The Frontier FTIR measurement range with a start wavelength of 2,000 nm is shown as well. Deviations are indicated as Δ . As in this scenario no extrapolation is implemented, all datasets are evaluated until 16,000 nm.

Table 12 – Variation of start wavelength without extrapolation. The start wavelength is varied within the ranges from 250 to 300 nm while no extrapolation is carried out. Therefore, the upper wavelength limit remains 16,000 nm in all scenarios. No difference in thermal emittance ($T = 923$ K) can be observed. Changing the start wavelength to 2,000 nm leads to a decrease of thermal emittance of around 2.5 % (deviation indicated as Δ).

λ_{start} [nm]	λ_{end} [nm]	CT [%]	IE [%]	CS [%]	DLR/ CIEMAT [%]
280	16,000	25.38	25.02	25.07	27.22
2,000	16,000	22.90	22.56	22.54	24.83
Δ		2.48	2.46	2.53	2.39

Similar to solar absorptance (see chapter 5.1.2), the variation of the start wavelength from 250 to 300 nm shows no deviation of the result value for thermal emittance. The use of a start wavelength of 2,000 nm such as proposed in Var4 in Table 8 (chapter 4.2.4) results in a decrease of the thermal emittance value. This variation leads to deviations of around 2.5 % for all institutes. A closer look at the calculation presented in chapter 5.2.2 (see especially Figure 21) provides an explanation for the variation of results such as seen in Table 12. Figure 24 shows a plot of the same data with special focus on the wavelength range from 0 to 5,000 nm.

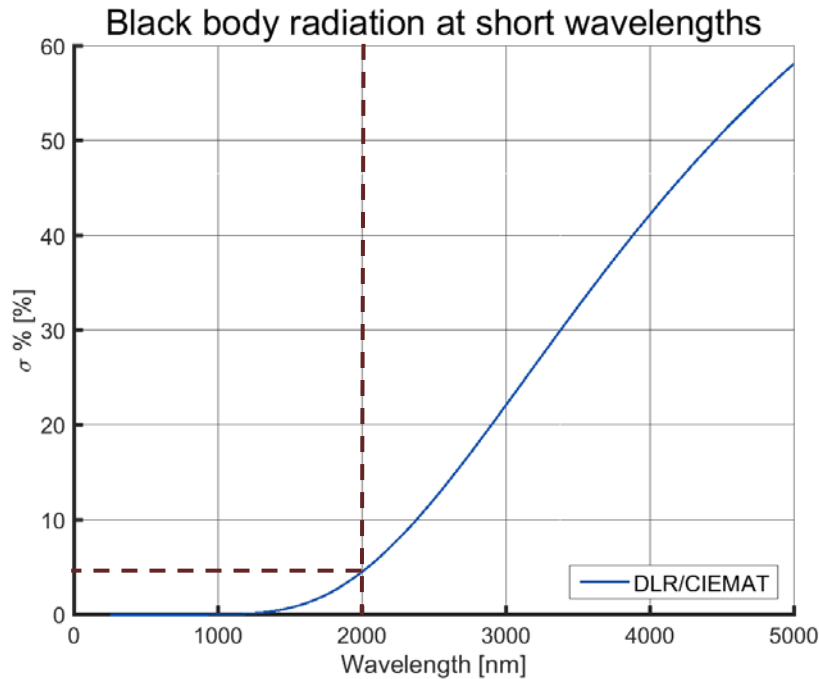


Figure 24 – Black body reference data (923K), zoom 0 to 5,000 nm. The dotted line represents the switch of the spectrophotometers at DLR/CIEMAT. There is no rise within the spectral range below 1,000 nm. Therefore, the changes of the start wavelength do not cause any variation of the calculation result.

It reveals that in the range of below 1,000 nm there is no increase in $\sigma\%$. This means that differences in small wavelengths are negligible because their share is constantly 0 % of the radiation of an ideal black body at 923 K. In contrast to that, the graph begins to increase at wavelengths greater than 1,000 nm. At 2,000 nm, the wavelength in question for Var4, 4.51 % of the radiation of an ideal black body is covered. As the black body reference data provides the denominator in Eq. 7, it causes a decrease in thermal emittance values derived for a wavelength range from 2,000 to 16,000 nm.

In the further analysis of measurement values, the lower limit of the wavelength range is considered negligible in the range of 250 to 300 nm and no further variation is carried out. The variation of the end wavelength leads to a decrease of thermal emittance values. Figure 25 shows the results for thermal emittance for a wavelength range from 280 nm to 16,000, 25,000 and 50,000 nm respectively. The extrapolation has been carried out with the ISO approach. Information on averages and standard deviations exclude the DLR/CIEMAT value.

Increasing the end wavelength from 16,000 to 50,000 nm causes a systematic drop in thermal emittance of 0.55 % (IE) to 0.62 % (DLR/CIEMAT). The average thermal emittance decreases from 25.16 % at 16,000 nm to 24.58 % at 50,000 nm, standard deviations are below 0.2 % in all scenarios.

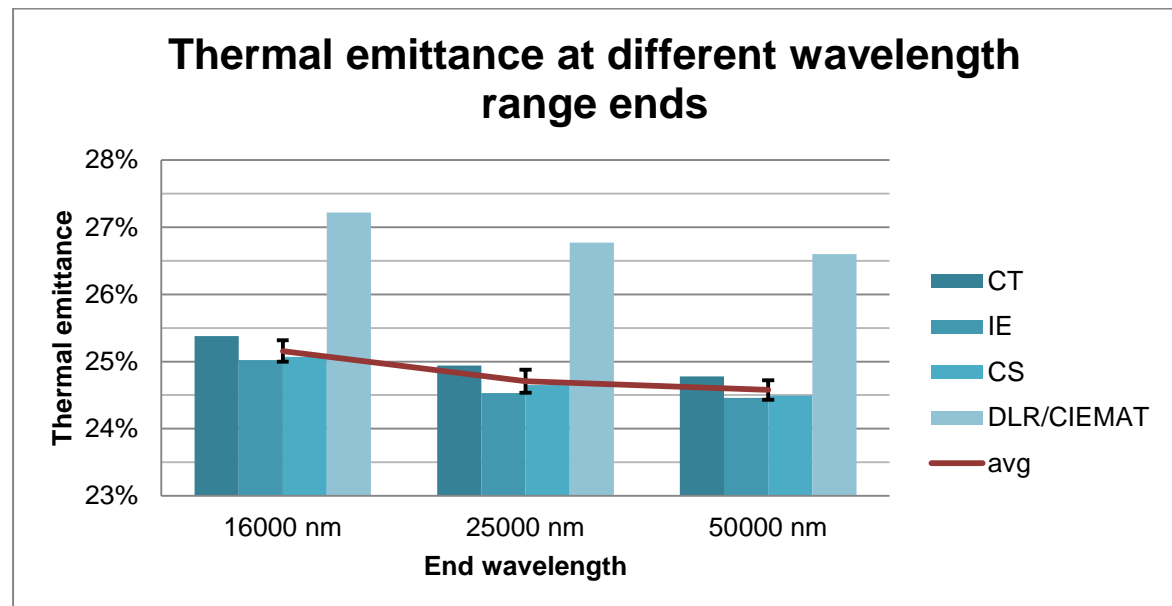


Figure 25 – Variation of end wavelength with extrapolation approach ISO. An increase of the end wavelength from 16,000 to 50,000 nm leads to a decrease of thermal emittance ($T = 923$ K) values. The average value presented does not include the DLR/CIEMAT value. Standard deviations (error bars) are below 0.2 %.

Figure 26 shows the data derived from the $\sigma\%$ calculation and focuses on the range from 10,000 to 20,000 nm.

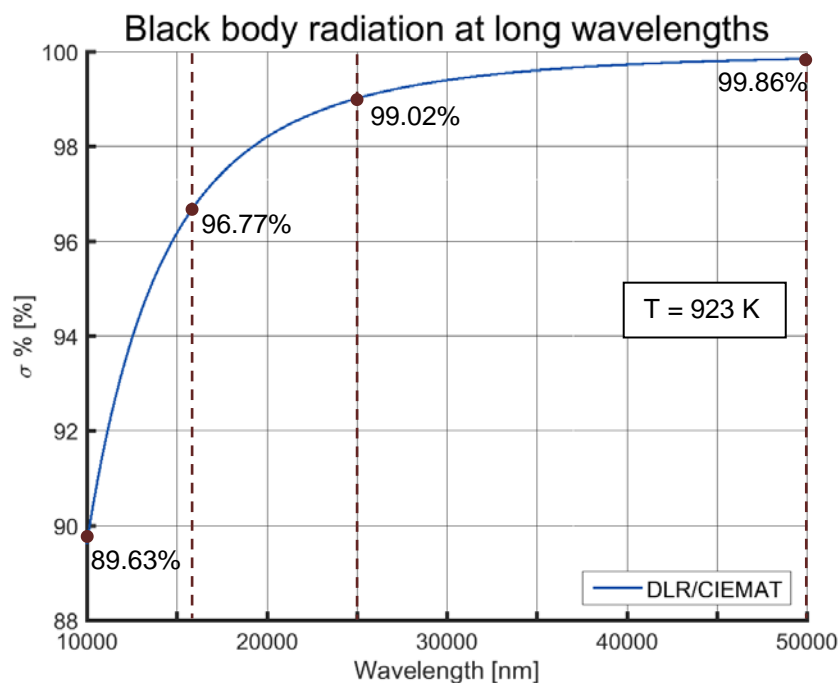


Figure 26 – Black body reference data (923 K), zoom 10,000 to 50,000 nm. There is a steep increase from around 90 % of the ideal black body's radiation to up to 99.86 %. This course of the graph points out the reason for the difference of thermal emittance results when varying the end wavelength from 16,000 to 50,000 nm.

5 Results and discussion

In comparison to the graph at small wavelengths, at long wavelengths the share of an ideal black body's radiation increases from 89.63 % (10,000 nm) to 99.86 % (50,000 nm). Up to 25,000 nm, the $\sigma\%$ -value reaches 99.02 % at 923 K. This is the reason for the decreases observed when varying the end wavelength from 16,000 to 25,000 nm (from 0.42 % for CS to 0.49 % for IE). The increase of $\sigma\%$ up to 99.86 % at 50,000 nm explains the deviation due to the variation of the end wavelength from 25,000 to 50,000 nm (from 0.15 % for CS to 0.18 % for IE).

Overall, it can be observed that greater wavelength ranges lead to smaller thermal emittance values, because in the case of selective solar absorber coatings great wavelengths coincide with high reflectance values. High values of $\rho_{\text{hem}}(\lambda)$ in Eq. 7 or Eq. 13 respectively lead to smaller numerators and result in smaller thermal emittance values. Table 13 shows the change in thermal emittance when using a common wavelength range from 280 to 50,000 nm after linear interpolation in steps of 1 nm.

Table 13 – Relative comparison of the 50,000 nm end wavelength scenario. The approach is compared to the datasets provided by the round robin partners. All values refer to 923 K and match the comparison data with less than 1 % deviation. For DLR/CIEMAT data, no comparison is carried out for initial values as the calculation process is defined during the round robin campaign. ISO extrapolation values are subtracted from initial values.

	λ_{start} [nm]	λ_{end} [nm]	CT [%]	IE [%]	CS [%]
Initial values	Variable as used by the institute		25.4	23.9	25.3
Δ end wavelength scenario	280	50,000	0.62	-0.45	0.81

The values presented correspond to the values presented in Table 11 as the ISO extrapolation approach is implemented. Deviations from the values provided by the round robin partners vary between ~0.5 and ~1 %. In the further analysis of data, the end wavelength will be set as 50,000 nm in order to apply the wavelength range proposed within the DIN EN ISO 22975-3.

5.2.5 Integral operators

After ensuring the same spectral resolution, measurement intervals and weighting for the processing of the different datasets, they are evaluated regarding different calculation methods. The variation of a summation (Eq. 13) and the integral calculation (Eq. 7) are of special interest. Additionally, two different MATLAB algorithms are tested for each approach. Table 14 presents the common result of these four calculation methods for the Raiselife round robin considered from 280 to 50,000 nm.

Table 14 – Result of different calculation methods. All values are calculated at 923 K using the DIN EN ISO 22975-3 extrapolation approach and therefore consider a wavelength range from 280 to 50,000 nm in steps of 1 nm. There is no difference in the different calculation approaches compared within the MATLAB script which is why the common result is presented only.

	CT [%]	IE [%]	CS [%]	DLR/ CIEMAT [%]
After integral calculation	24.78	24.35	24.49	26.60

The variation between different MATLAB algorithms does not lead to a variation in the result for the thermal emittance calculation. Two different sum calculation approaches (*sum* and *trapz*) provide the same thermal emittance value. The same happens with the two integration approaches tested (*inetr* and *quadgk*). Additionally, the calculations with the sum algorithms and the ones using the integrals result in the same value. Table 14 shows the values for the wavelength range from 280 to 50,000 nm extrapolated according to DIN EN ISO 22975-3. Other wavelength ranges reveal the same observation.

All values now refer to a temperature of 923 K (650 °C) and a wavelength range from 280 to 50,000 nm, extrapolated according to DIN EN ISO 22975-3. In all cases data has been processed using the same black body reference spectrum according to Planck's law (Eq. 8, chapter 3.2.2).

5.3 Discussion and improvements

As the reproducibility of solar absorptance has already been proven in chapter 5.1.3, this chapter focuses on the discussion of thermal emittance results taking into account the different approaches for the correction of the internal measurement mismatch (chapter 5.2.1) as well as the implementation of the Raiselife round robin campaign (chapters 5.2.2 to 5.2.5). First of all, common processing of data needs to be executed to guarantee the reproducibility of results.

5.3.1 Standardisation of calculation

Table 15 points out the different steps performed by the round robin partners during the process of determining thermal emittance. Only similar conditions enable a derivation of a basis for the evaluation of the mismatch correction. This targets a corrected average value that represents a basis for the comparison with the post-processed DLR/CIEMAT data.

Table 15 – Measurement and calculation processes of the round robin partners. The greatest difference is observed in the measurement resolutions and the wavelength ranges considered for the thermal emittance calculation.

		CT	IE	CS	DLR/ CIEMAT	IA
Measurement		Spectral measurement principle (chapter 3.3)				
	Spectrophotometer(s)	V	V	V	V	
	Portable device					V
		Spectral measurement resolution				
	UV-VIS-NIR [nm]	10	variable	10	4	1
	(N)IR [nm]	~2		3 rep. 4	5	?
Calculation		Black body exitance reference temperature (chapter 5.2.2)				
	Planck's law (923 K)	V	V	V	V	
	Planck's law (300 K)					V
		Extrapolation method (chapter 5.2.3)				
	IE		V			
	ISO					
		Wavelength range (according to Table 8, chapter 4.2.4)				
	Var1	V			V	?
	Var2			V		
	Var3		V			
		Integral calculation (chapter 5.2.5)				
	Summation	V	V	V	V	?
	Initial value [%]	25.4	23.9	25.3		8.8

Figure 27 gives an overview of the different calculation approaches for the thermal emittance of the round robin sample IF09 at 923 K executed within this thesis. Calculation results and their standard deviations are presented (referred to as stdev). The methods indicated refer to the following approaches:

- **Before processing:** initial values provided by the institutes themselves determined under the conditions presented in Table 15,
- **Extrapolation IE:** extrapolation of data to 50,000 nm with the mean value of the range from 12,000 to 14,000 nm (execution chapter 5.2.3),

5 Results and discussion

- **Extrapolation ISO:** extrapolation of data to 50,000 nm with the last available value as constant value (execution chapter 5.2.3) and
- **Short range:** consideration of the wavelength range from 280 to 16,000 nm (execution chapter 5.2.4).

The extended wavelength scenario (chapter 5.2.4) and the values obtained from the integral calculation (chapter 5.2.5) are not included explicitly as they equal to the extrapolation ISO values. All approaches have been applied to interpolated data in steps of 1 nm.

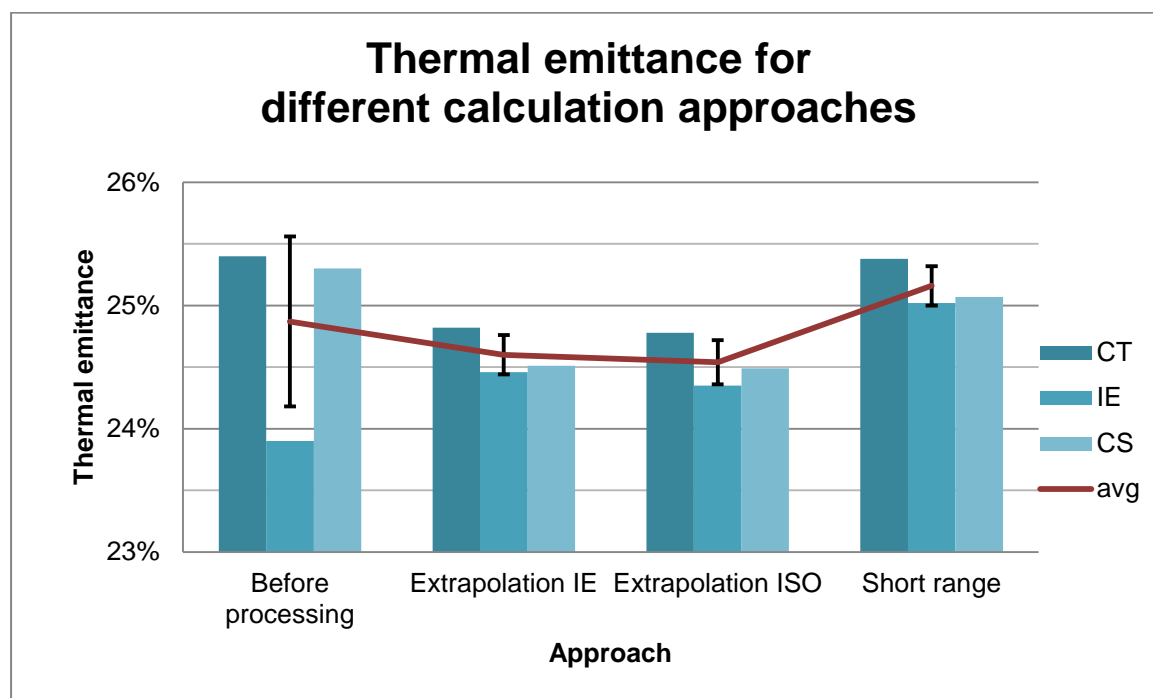


Figure 27 – Overview: thermal emittance calculation approaches and their results. For each approach, the absolute results as well as the standard deviation (presented as error bars) within the different datasets is considered. DLR/CIEMAT values are presented but not included within the calculation for the average and the standard deviation. All values refer to a temperature of 923 K.

As already described for solar absorptance (chapter 5.1.3), there are no absolute reference values available for thermal emittance as a function of temperature. Consequently, reproducibility is examined. High reproducibility is indicated by small standard deviations. The smallest deviations of 0.16 % are observed for the extrapolation with the IE approach and the short range scenario. ISO extrapolation shows a similar standard deviation of 0.18 %. Hence, the ISO extrapolation approach seems more promising for the application at selective coatings as its values coincide with the CS reflectance measurement used as a means to evaluate the extrapolations (Figure 22, chapter 5.2.3). Therefore, the use of the summation in combination with the ISO extrapolation approach is recommended. Eq. 16 represents the most recommendable approach for the calculation of thermal emittance. However, it needs to be considered that the MATLAB script for the ISO approach writes the last value available at 16,000 nm (25,000 nm for CS) up to 50,000 nm. In

case of noisy data, this last value could be biased and therefore the extrapolation function applies a bias. It is recommendable to check the extrapolation graphs provided by MATLAB in order to identify possible biases induced by this approach.

$$\varepsilon_{th}(T) = \frac{\sum_{280\text{ nm}}^{50000\text{ nm}} [1 - \rho_{hem}(\lambda)] * E_{BB}(\lambda, T) * d\lambda}{\sum_{280\text{ nm}}^{50000\text{ nm}} E_{BB}(\lambda, T) * d\lambda} \quad \text{Eq. 16}$$

Figure 28 shows the final comparison of the thermal emittance values from the round robin campaign. Values *before processing* refer to the initial values provided by the institutes as presented in Table 15. Hence, no DLR/CIEMAT data is included. *After processing* refers to the implementation of Eq. 16. Deviations are indicated as Δ .

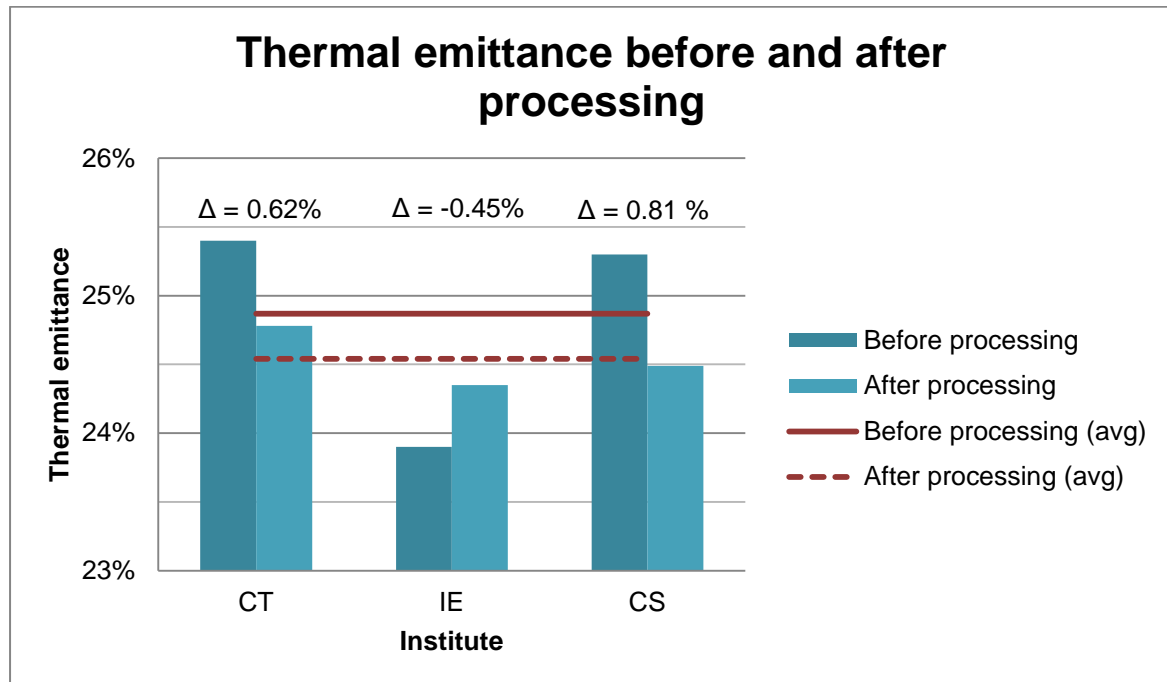


Figure 28 – Thermal emittance values at 923 K before and after processing at PSA. The deviation of the values (indicated above as Δ) ranges from 0.45 % (IE) to 0.81 % (CS). IE is the only value that increases due to common processing. The average thermal emittance decreases from 24.87 % to 24.54 %.

CT and CS values show a drop in thermal emittance while the IE value increases. The average decreases from 24.87 % to 24.54 % and the standard deviation within the values can be reduced from 0.68 % to 0.18 %. This proves the reproducibility of the spectral measurement of the Raiselife round robin sample IF09 after common treatment. Figure 29 summarises the processing steps exercised within the campaign.

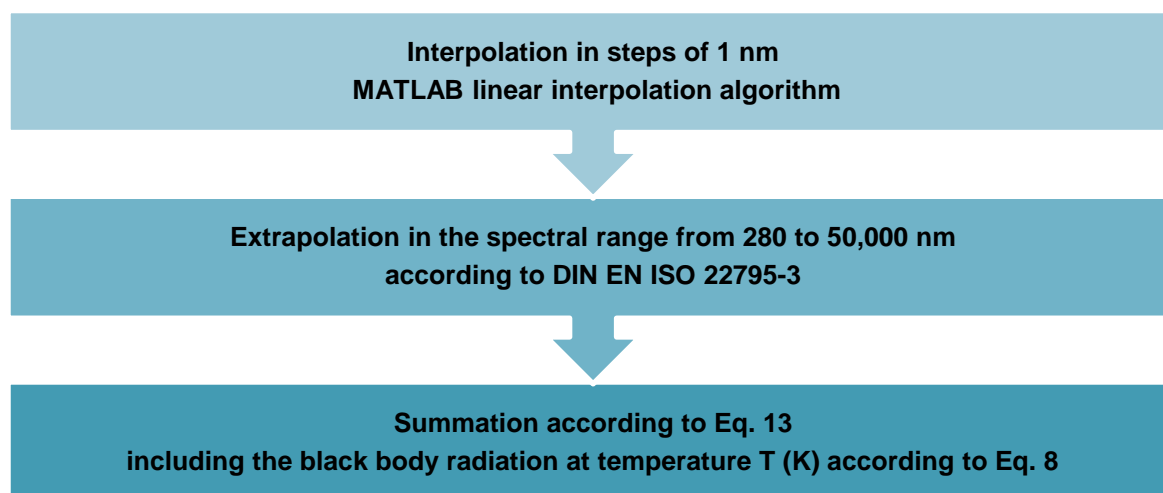


Figure 29 – Flow chart of thermal emittance data processing within the Raiselife round robin campaign. All values have been linearly interpolated in steps of 1 nm before implementing the extrapolation according to DIN EN ISO 22795-3. Thermal emittance is calculated according to the summation presented in Eq. 13.

The reflectance measurement values provided by the partner institutes are linearly interpolated in steps of 1 nm and extrapolated according to the DIN EN ISO 22795-3 approach in the wavelength range of 280 to 50,000 nm. Thermal emittance is calculated with Eq. 13 at a temperature of 923 K. For the latter, the black body radiation according to Planck's Law (Eq. 8, chapter 3.2.2) is included.

5.3.2 Frontier FTIR post-processing

After the implementation of different approaches in the course of the Raiselife round robin campaign, a new routine for Frontier FTIR raw data treatment can be derived. Figure 30 shows a flow chart of the most recommendable post-processing approach for the raw Frontier FTIR spectral data according to mismatch correction approach 2 (see Figure 11, chapter 4.2.1).

The most promising approach for the correction of the internal mismatch between the Lambda 1050 and the Frontier FTIR data is post-processing the raw Frontier FTIR reflectance values according to approach 2. Using the offset with the corrected results of the Lambda 1050 spectrophotometer in the common wavelength range from 2,000 to 2,500 nm as presented in Eq. 11 (chapter 4.2.1) enables an extrapolation of the deviation. The mean deviation can be extrapolated in the range from 2,500 to 16,000 nm according to Eq. 12. This approach permits the approximation of Frontier FTIR reflectance values to the measurement values of the round robin partners (Figure 19, chapter 5.2.1).

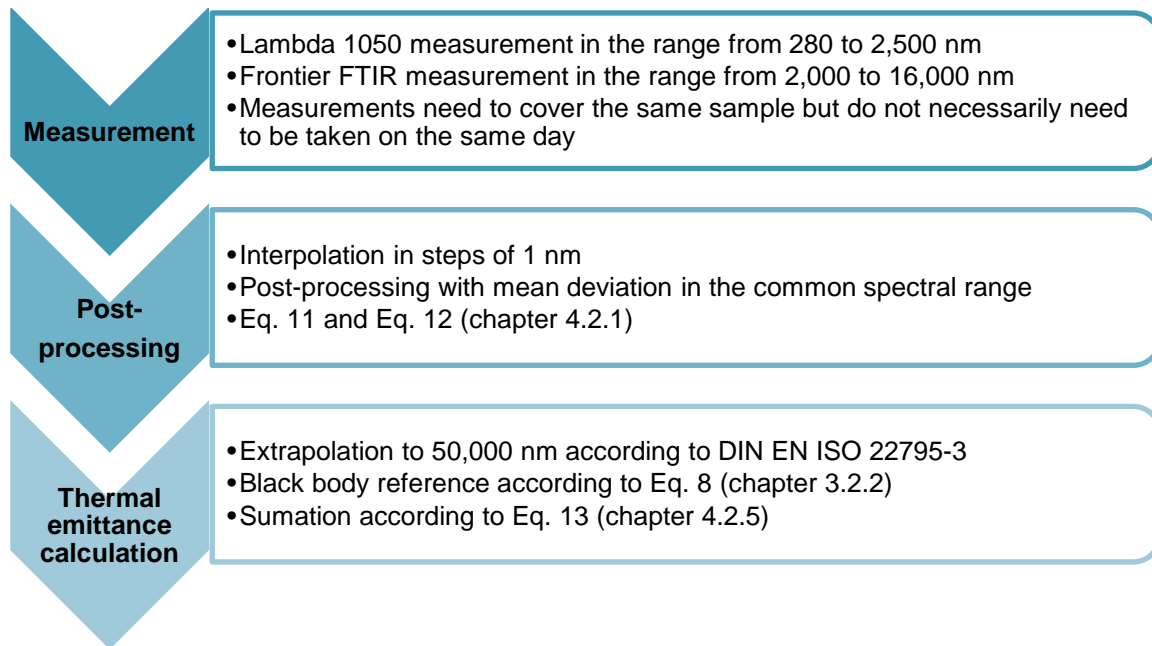


Figure 30 – Flow chart of recommended post-processing of Frontier FTIR raw reflectance measurement data. The measured spectral data is treated according to mismatch correction approach 2 (Figure 11, chapter 4.2.1). Thermal emittance is then calculated with Eq. 13 (chapter 4.2.5).

Figure 31 shows a comparison of the DLR/CIEMAT thermal emittance values and average value such as seen in Figure 28. DLR/CIEMAT values are obtained from the reflectance dataset after applying the mismatch correction according to Figure 30. The deviation between the DLR/CIEMAT calculated thermal emittance and the average round robin value is 2.06 %. This means that thermal emittance calculated from the corrected Frontier FTIR values results in higher values than the average round robin results. A look the graph of IR spectral data used for the calculation (Figure 19, chapter 5.2.1) reveals that the DLR/CIEMAT values tend to be smaller than the reflectances measured by the partner institutes. In the calculation of thermal emittance according to Eq. 7 or Eq. 13 respectively, smaller $\rho_{\text{hem}}(\lambda)$ values lead to greater numerators and consequently to greater thermal emittance results.

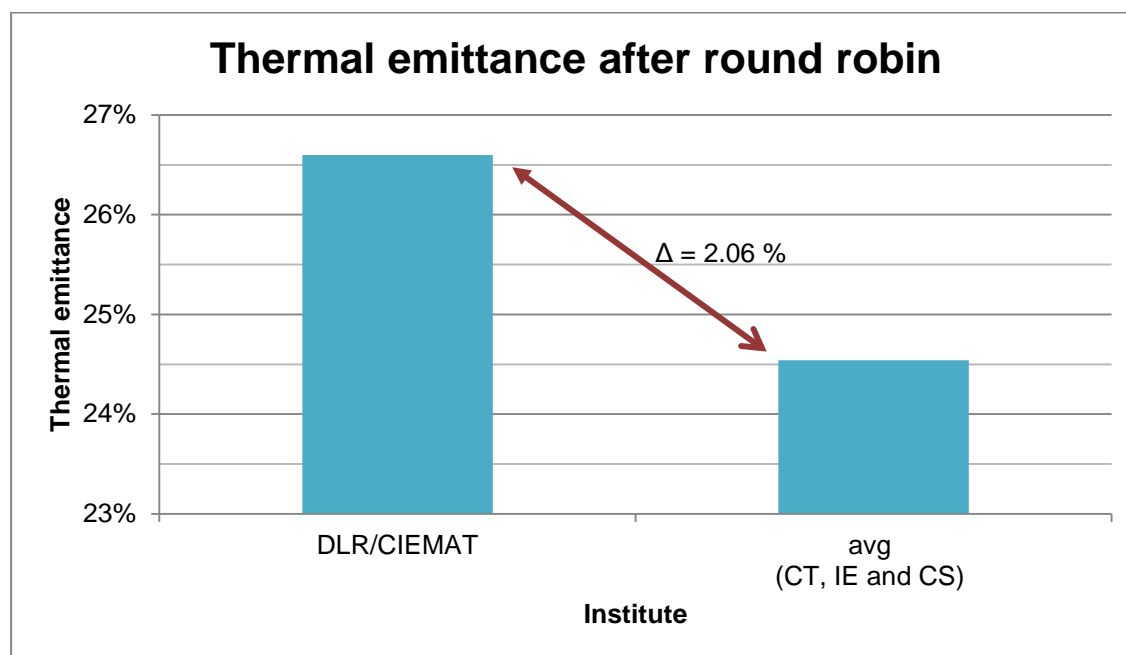


Figure 31 – Deviation of DLR/CIEMAT thermal emittance from round robin average for the different calculation approaches at 923 K. DLR/CIEMAT data refers to reflectance values after applying the mismatch correction and the reference value is the average of the round robin participants such as presented in the table above.

The approach presented in Figure 30 offers a possibility for the post-processing of the datasets available from Frontier FTIR for all samples that have been measured with the Lambda 1050 spectrophotometer as well.

5.3.3 New Frontier FTIR measurement routine

For future measurements, the use of a reference standard calibrated in the spectral range until at least 16,000 nm is recommendable. As shown in Figure 20 and Figure 35 (chapter 5.2.1), regular baseline measurements offer the option of correcting the raw Frontier FTIR data with calibrated reference data. This leads to the derivation of a new measurement routine with the steps according to mismatch correction approach 3 (Figure 11, chapter 4.2.1) presented in the flow chart in Figure 32 and visualised in Figure 33.

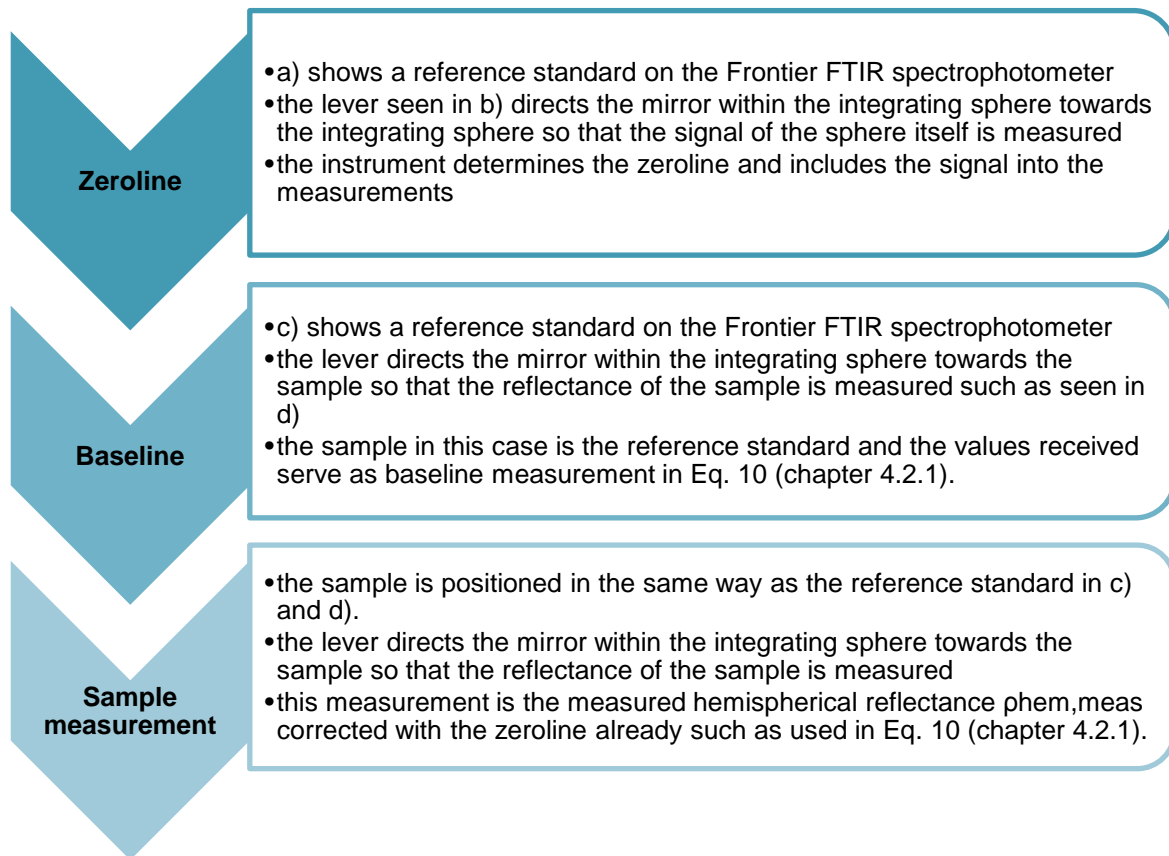


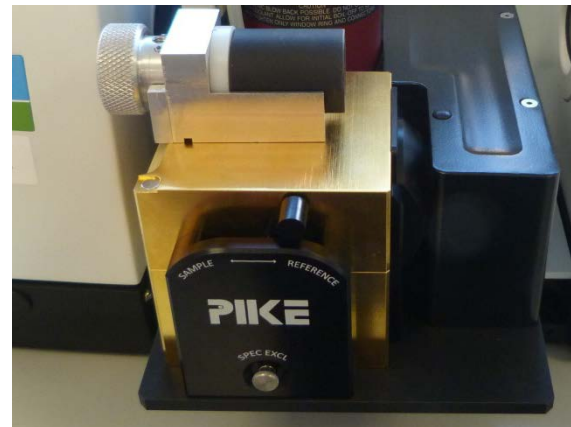
Figure 32 – Flow chart new measurement routine. The steps for the detection of the zeroline, the baseline signal and the final measurement of the sample are documented in Figure 33. Spectral measurement values are treated according to Eq. 10.

The new routine would enable the calculation of $\rho_{\text{hem}}(\lambda)$ in the IR range without the need of Lambda 1050 data for the same sample and hence offers more independent measurements

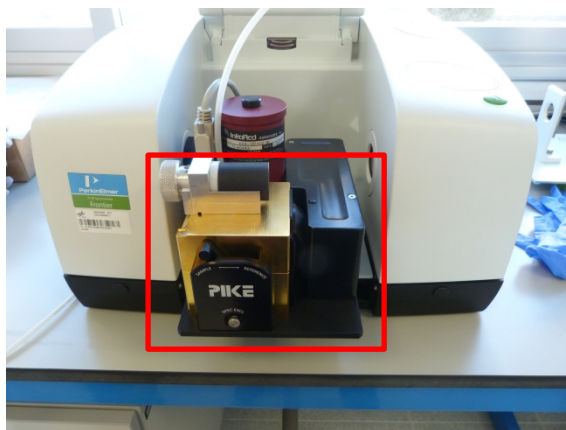
a)



b)



c)



d)



Figure 33 – Overview lever positions used for new measurement routine. All pictures are taken with a black diffuse sample. a) shows the lever in the reference position. The mirror in the integrating sphere is directed to the sphere itself. The data obtained serves as zeroline information. b) provides a zoom in. c) shows the lever in the sample position. The mirror is directed towards the diffuse sample and its reflectance is measured. The data obtained serves as baseline information. d) shows a zoom in.

The zeroline and baseline measurements should be repeated for every coating in consideration. This means that one determination of the variables can be used for the measurement of three coated tubes (chapter 2.2).

6 Summary and outlook

In the course of this thesis, several approaches for the analysis of a round robin campaign within the Horizon 2020 Raiselife project have been implemented. After the successful correction of an internal mismatch, calculations for the solar absorptance and thermal emittance of solar absorber coatings have been applied. The results are summarised within this chapter. An outlook for the further progress of the Raiselife WP3 at PSA will be derived from the analysis.

When examining the round robin initial values for solar absorptance and thermal emittance, it has been observed that the different round robin participants' measurement and calculation approaches differ (Table 3 and Table 4, chapter 3.3). This points out the necessity of defining a common standard that has been implemented with the data processing according to Figure 16 and Figure 29 (chapters 5.1.3 and 5.3 respectively). The common processing of the institutes' spectral measurement values lead to the confirmation of the reproducibility of the measurement process. Considering solar absorptance, this has been proven for all institutes while for thermal emittance this conclusion applies to all institutes but IA, as the institute did not provide spectral data in the IR range, but an integrated value at a different reference temperature.

The results presented in the course of chapter 5 enable a new consideration of the parameters used for the calculation of thermal emittance (Eq. 1, chapter 2.1). Table 16 shows an update of Table 2 (chapter 2.3), changes are marked in red.

Table 16 – Thermal efficiency parameters and their optimisation potential update. The results achieved during this thesis verified solar absorptance values determined with the Lambda 1050 spectrophotometer and enables a reduction of the measurement error in thermal emittance.

Parameter	Status quo	Optimisation potential
σ	Physical constant	None
Q_{sol}	Measurement principle verified in the course of a prior master thesis	None
α_s	<i>Verified during round robin campaign</i>	<i>None</i>
T_{abs}	Measurement principle improved within prior master thesis, no overheating of the samples	Exact skin temperature unknown
ϵ_{th}	<i>Spectral mismatch corrected, approximation to round robin value achieved by postprocessing according to ISO 22975-3</i>	<i>Implementation of new measurement routing with calibrated reference standard</i>

Solar absorptance values determined with the Lambda 1050 spectrophotometer have been verified in the course of the round robin campaign (chapter 5.1). There is no more optimisation potential. Thermal emittance values determined with the Frontier FTIR spectrophotometer approaches the average round robin value through post-processing, with a remaining systematic error of 2.1 %. The deviation within the round robin thermal emittance values has been reduced with common processing (Figure 29, chapter 5.3.). The new measurement routine described in Figure 32 (chapter 5.3) promises a further reduction of the deviation once a calibrated reference standard is available at OPAC for the NIR-MIR wavelength range. This will also enable more independent measurements with the Frontier FTIR spectrophotometer, as Lambda 1050 reference data from the same specimen is needed for the postprocessing. The signal's noise (Figure 13, chapter 4.2.1) could not be eliminated yet. A first test of the smoothing of data leads to cleaner graphs but does not result in a further correction of thermal emittance values (see documentation in Appendix D). Still, the determination of thermal emittance with a 2.1%-deviation already allows a new evaluation of the coatings' thermal efficiencies according to Eq. 1.

As the installation of an infrared camera at the test dish is planned, further investigation will also focus on the contactless verification of the temperature measurement as described in chapter 2.3. The implementation of an infrared measurement device however requires the specification of the thermal emittance of the area in question in order to configure the camera. The approach worked out and evaluated within this thesis (Figure 30, chapter 5.3) allows the determination of the input value required. This planned step will not change the calculation results as temperature is already considered to be 923 K (650 °C) but will help to guarantee that the specimens are exposed at the temperature desired.

A precise determination of thermal efficiency is crucial for the evaluation of the coatings developed within the Raiselife project. Correct values enable a comparison of the four coatings in question and the identification of the best suitable material as well as of possible failure mechanisms of the coatings. The knowledge about weaknesses provides the possibility for the further improvement of the materials' durability. More efficient absorber coatings in CSP applications promise a decrease of LCOC and consequently of LCOE. Lower costs lead to a higher cost-competitiveness of concentrating solar power applications within the global energy market's shift towards renewable energies.

7 Bibliography

- [1] National Institute of Standards and Technology (NIST), "The NIST Reference on Constants, Units, and Uncertainty," 25 06 15. [Online]. Available: <https://physics.nist.gov/cuu/Constants/>. [Accessed 07 12 17].
- [2] ASTM International, "E 903 - 96: Standard Test Method for Solar Absorptance, Reflectance, and Transmittance of Materials Using Integrating Sphere," ASTM International, West Conshohocken, 1996.
- [3] Mecherikunnel, A. T. et al., "Data on total and spectral solar irradiance," *Applied Optics*, vol. 22, no. 9, pp. 1354-1359, 1983.
- [4] Ho, C. K. et al., "Characterization of Pyromark 2500 Paint for High-Temperature Solar Receivers," *Journal of Solar Energy Engineering*, vol. 136(1), no. SOL-12-1292, 2013.
- [5] Duffie, J. A. and Beckmann, W. A., *Solar engineering of thermal processes*, Hoboken, New Jersey: John Wiley & Sons, Inc., 2006.
- [6] ASTM International, "E 691 – 05: Standard Practice for Conducting an Interlaboratory Study to Determine the Precision of a Test Method," ASTM International, West Conshohocken, 2005.
- [7] Pfänder, M., "Pyrometrische Temperaturmessung an solarthermischen Hochtemperatur-Receivern," Deutsches Zentrum für Luft- und Raumfahrt, Almería, 2006.
- [8] Desmond, J., "Understanding Solar Flux: Science vs. Science Fiction," BrightSource Energy, Inc, 19 08 2014. [Online]. Available: <http://www.brightsourceenergy.com/understanding-solar-flux-science-vs-science-fiction-1>. [Accessed 24 01 2018].
- [9] Lazard, "Lazard's levelized cost of energy analysis - version 11.0," 02 11 2017. [Online]. Available: <https://www.lazard.com/media/450337/lazard-levelized-cost-of-energy-version-110.pdf>. [Accessed 25 01 2018].
- [10] New Energy Update, "ACWA Power scales up tower-trough design to set record-low CSP price," 20 09 2017. [Online]. Available: <http://newenergyupdate.com/csp-today/acwa-power-scales-tower-trough-design-set-record-low-csp-price>. [Accessed 25 01 2018].
- [11] Sutter, F., "Raising the Lifetime of Functional Materials for Concentrated Solar Power Technology," [Online]. Available: <https://www.raiselife.eu/activities/index.php>. [Accessed 25 19 2017].
- [12] Heller, P., *The Performance of Concentrated Solar Power (CSP) Systems*, Duxford: Woodhead Publishing, 2015.
- [13] Office of Energy Efficiency & Renewable Energy (U.S. Department of Energy), "Concentrating Solar Power Basics," 20 08 2013. [Online]. Available: <https://energy.gov/eere/energybasics/articles/concentrating-solar-power-basics>. [Accessed 09 11 2017].
- [14] Roldán Serrano, M.I., "Concentrating Solar Thermal Technologies," in *Concentrating Solar Thermal Technologies. Green Energy and Technology*, Cham, Springer, 2017, pp. 11-24.
- [15] C. K. Ho, "Advances in central receivers for concentrating solar applications," *Solar Energy*, vol. 152, pp. 38-56, 2017.

7 Bibliography

- [16] Ho, C. K. et al., "Levelized Cost of Coating (LCOC) for selective absorber materials," *Solar Energy*, vol. 108, pp. 315-321, 2014.
- [17] Caron, S. et al., "Accelerated Ageing of Solar Receiver Coatings: Experimental Results for T91 and VM12 Steel Substrates," in *SolarPACES 2017*, Santiago de Chile, 2017.
- [18] Röger, M. et al., "Techniques to Measure Solar Flux Density Distribution on Large-Scale Receivers," *Solar Energy Engineering*, vol. 136, no. 3, p. 10, 2014.
- [19] Hanssen, L. et al., "Infrared Optical Properties of Materials," 02 2015. [Online]. Available: <http://dx.doi.org/10.6028/NIST.SP.250-94>. [Accessed 27 10 2017].
- [20] National Renewable Energy Laboratory (NREL), "Reference Solar Spectral Irradiance: ASTM G-173," [Online]. Available: <http://rredc.nrel.gov/solar/spectra/am1.5/astmg173/astmg173.html>. [Accessed 06 12 2017].
- [21] Caron, S., "Accelerated aging of thick glass second surface silvered reflectors under sandstorm conditions. Student Thesis," 16 01 2012. [Online]. Available: diva2:519165. [Accessed 27 01 2018].
- [22] International Organization for Standardization, "DIN EN 22795-3: Solar energy — Collector components and materials — Part 3: Absorber surface durability," International Organization for Standardization, Geneva, 2014.
- [23] European Commission, "What is Horizon 2020?," [Online]. Available: <https://ec.europa.eu/programmes/horizon2020/en/what-horizon-2020>. [Accessed 25 09 2017].

8 Appendix

A	Digital content.....	X
B	Raiselife project	X
C	Further evaluation of mismatch approach 3.....	XI
D	Implementation of the smooth function	XII
E	Organisation.....	XIV

A Digital content

- MATLAB figures
- Project workflow (Gantt)
- Thesis structure (Mindjet MindManager)

B Raiselife project

In the year 2014 the European Union launched the project Horizon 2020. It “is the biggest EU Research and Innovation programme ever with nearly €80 billion of funding available over 7 years (2014 to 2020) – in addition to the private investment that this money will attract. It promises more breakthroughs, discoveries and world-firsts by taking great ideas from the lab to the market.” [23]

RAISELIFE (short for Raising the Lifetime) is a project within the Horizon 2020 programme and aims at “raising the lifetime of [...] concentrated solar power (CSP) technologies” [11]. The five key functional materials that have been determined to focus on are:

- protective and anti-soiling coatings for primary reflectors,
- very high-reflective surfaces for heliostats,
- high-temperature secondary reflectors,
- receiver coatings and
- corrosion resistant high-temperature metals and coatings for molten salts. [11]

Figure 34 shows a PERT chart of the different workflows within the project. The work packages (WP) are derived from the five key functional materials mentioned before. It becomes clear that the investigation on primary reflector coatings (WP1), high-temperature mirrors for secondary concentrators (WP2), receiver coatings (WP3) and corrosion resistant high-temperature metals and coatings for molten salt (WP4) are run parallel. The analysis of the impact of degradation on performance of components and systems (WP5) depends on the results of the work packages mentioned before. The results of these five work packages flow into the dissemination and exploi-

tation (WP6) while the management and coordination (WP7) of the project acts independently as a means to guarantee the quality of results achieved by the project.

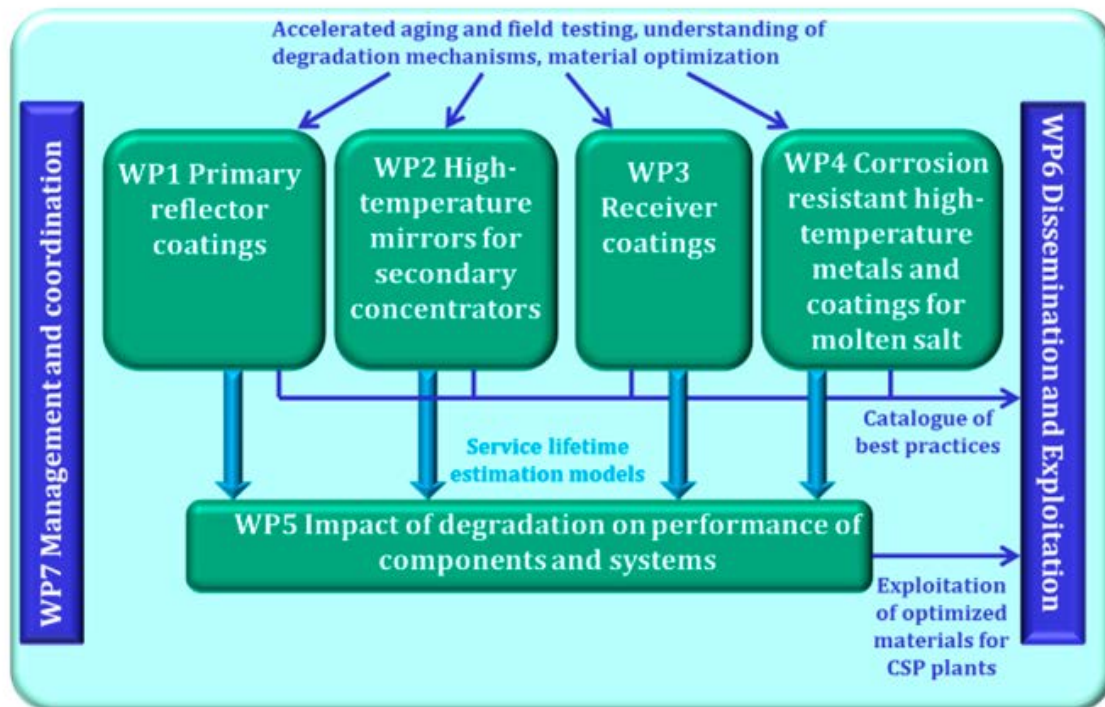


Figure 34 – Raiselife PERT chart lining out the workflows within the project [11]. WP1 to WP4 act parallel whereas WP5 depends on their results. WP6 collects the results of WP1 to WP5 while WP7 coordinates the project independently.

The improvement of CSP technologies does not only promise an increase of efficiency, but also a decrease of costs by raising the durability of different components. Larger maintenance intervals help reducing maintenance costs. Therefore the project is of special interest for all kinds of possible investors in CSP power plants.

C Further evaluation of mismatch approach 3

In the course of this calculation, the Lambda 1050 and the Frontier FTIR data is compared as represented in Eq. 17.

$$\Delta_{WS} = \rho_{hem, \text{Lambda1050}} - \rho_{hem, \text{Frontier FTIR}} \quad \text{Eq. 17}$$

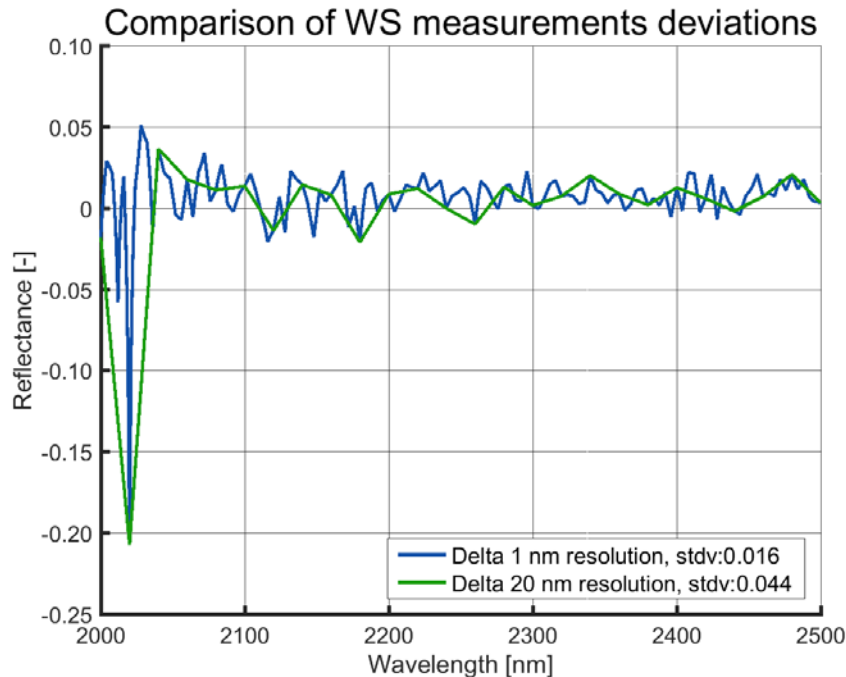


Figure 35 – Difference between processed data of WS measurements with Lambda 1050 and Frontier FTIR in resolutions of 20 nm, representing the raw data, and 1 nm as for interpolated data. The interpolation enables a reduction of the standard deviation within the data in consideration.

Especially the wavelength range between 2,000 and 2,050 nm shows deviations due to the high noise of the Frontier FTIR data. After that, both graphs provide values oscillating around 0. This means that the Frontier FTIR values are smaller than the Lambda 1050; Figure 20 proves that. Figure 35 shows that the general course of the graph does not change when the resolution is increased. The interpolated values lead to a curve with higher noise, but also enable a reduction of the standard deviation. It is reduced from 4.4 % (20 nm resolution) to 1.6 % (1 nm resolution).

D Implementation of the smooth function

In order to evaluate if the smoothing of the Frontier FTIR signal enables a reduction of the measurement error, different MATLAB algorithms are tested. Figure 36 presents the Frontier FTIR reflectance values after the application of the mismatch correction. Five different MATLAB *methods* have been applied and are visualised in the graph as well. The *span* factor is set 0.1 for all approaches as recommended in the MATLAB help documentation.

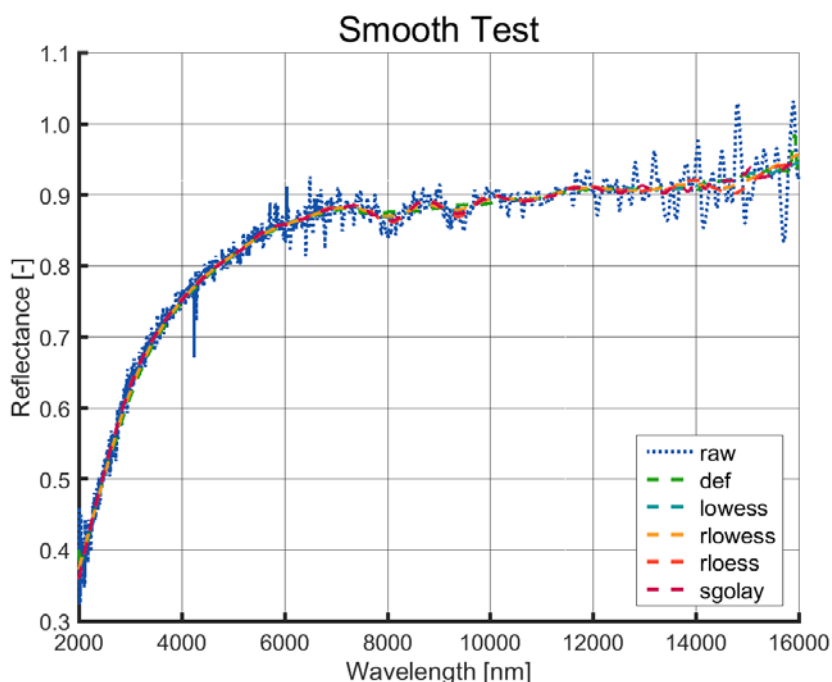


Figure 36 – Frontier FTIR data and MATLAB smooth functions. All approaches lead to a reduction of the noise in the corrected Frontier FTIR values. *Span* variable is set 0.1 for all methods.

All five MATLAB smooth *methods* enable a reduction of the noise without falsifying the course of the graph significantly. *Span* values describe the window size for the smoothing. Great values consequently risk losing data because of large smoothing intervals while too small values might cause no smoothing at all. Hence, they have been varied from 0.05 to 0.2 and the resulting reflectance values have been progressed with the thermal emittance MATLAB script.

Table 17 – Thermal emittance of DLR/CIEMAT data with different MATLAB algorithms regarding smooth *methods* and *spans*. The variation of span does not lead to a significant change in results. All values have been calculated for a wavelength range from 2,000 to 16,000 nm at 923 K.

Span	Moving	lowess	rlowess	rloess	sgolay
0.05	24.83%	24.93%	24.93%	24.88%	24.82%
0.077	24.83%	25.08%	25.08%	24.94%	24.82%
0.1	24.83%	25.24%	25.24%	25.01%	24.81%
0.2	24.83%	26.03%	26.03%	25.17%	24.84%
avg	24.83%	25.08%	25.08%	24.94%	24.82%
stdev	0.00%	0.12%	0.12%	0.05%	0.00%

Standard deviations for the variation of the *span* within one smooth *method* range from 0 % (moving and sgolay) to 0.12 % (lowess and rlowess) around the average thermal emittance values

from 24.82 % (sgolay) to 25.08 % (lowess and rlowess). Without smoothing, DLR/CIEMAT reflectance values result in a thermal emittance of 24.83 % for the wavelength range of 2,000 to 16,000 nm while the other institutes' data results in values between 22.54 % (CS) and 22.90 % (CT) as presented in Table 12 (chapter 5.2.4). No significant improvement of the DLR/CIEMAT result has been achieved with smoothed data.

E Organisation

Main workflows during this project have been organised using a Gantt chart within Microsoft Project. The chart is provided in the digital content. Smaller exercises have been listed up in a table generated with Microsoft Excel. Table 18 shows an abstract of the Excel sheet. It allows marking the status of the single process in steps of 25, 50, 75 and 100 % and enables a quick overview of the recent tasks.

Table 18 – Overview Project organisation with Microsoft Excel. Tasks are given a due date and organised in steps of 25, 50, 75 and 100 %.

Task	Due	25%	50%	75%	100%
put samples into condensation chamber	06.10.17	x	x	x	x
FTIR measurement VM12 after Condensation	11.10.17	x	x	x	x
Masterfile after 150 cycles complete	09.10.17	x	x	x	x
implement mismatch statistics	09.10.17	x	x	x	x
mounting T22 at dish	20.10.17	x	x	x	x
microscope measurements T22 after 25 cycles	07.11.17	x	x	x	x
Interpolation Round Robin Ebb curves MATLAB	start 11.12.17	x	x	x	x
MATLAB loop plot spectral data	21.12.2017	x	x	x	x
Mismatch corr calc Excel	15.12.2017	x	x	x	x
test new measurement routine	19.12.2017	x	x	x	x
Implement mismatch corr in MATLAB	20.12.2017	x	x	x	x
Sum vs integral Eth round robin MATLAB	22.12.2017	x	x	x	x
Extrapolation IE vs IO MATLAB	22.12.2017	x	x	x	x
Smooth Eth MATLAB	25.01.2018	x	x	x	x

Furthermore, a mind map generated with Mindjet MindManager has been used for structuring the main chapters of this thesis. The different approaches for the round robin campaign presented in chapter 4 and exercised in chapter 5 have been listed in order to generate an overview of the calculations that need to be executed. Already implemented ones have been marked yellow. Figure 37 presents an overview of the structure tree generated with the programme.

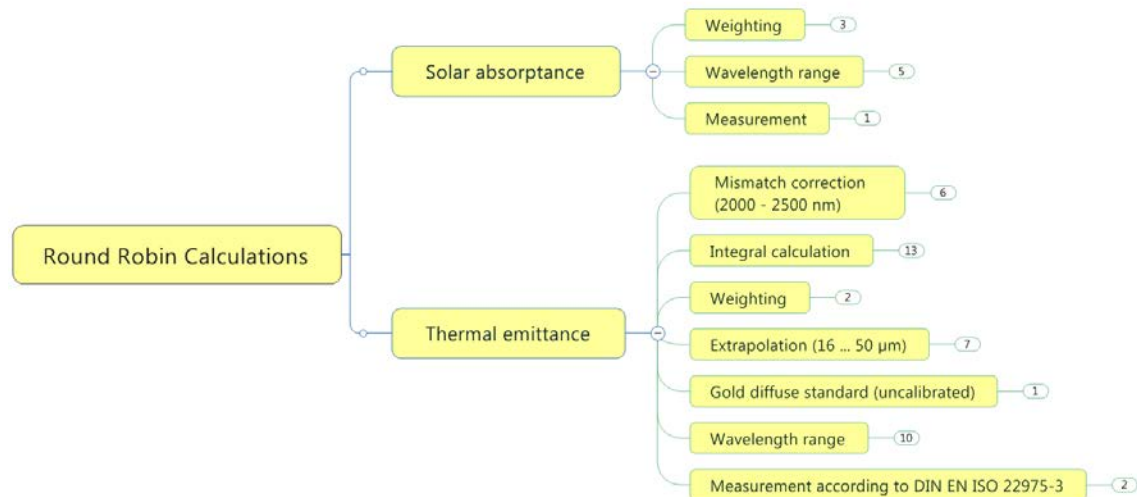


Figure 37 – Overview Mindjet MindManager. Main tasks used for structuring of this thesis. All tasks have been exercised and are marked in yellow.

Each branch of the structure can be expanded in order to derive a view of the tasks contained in the different chapters. Figure 38 shows the details provided by Mindjet MindManager when expanding some branches. In this example, the tasks for Mismatch Correction, Integral calculation and Extrapolation are shown. All points have been implemented already which is why they are marked in yellow.

The Mindjet MindManager file is provided within the digital content.

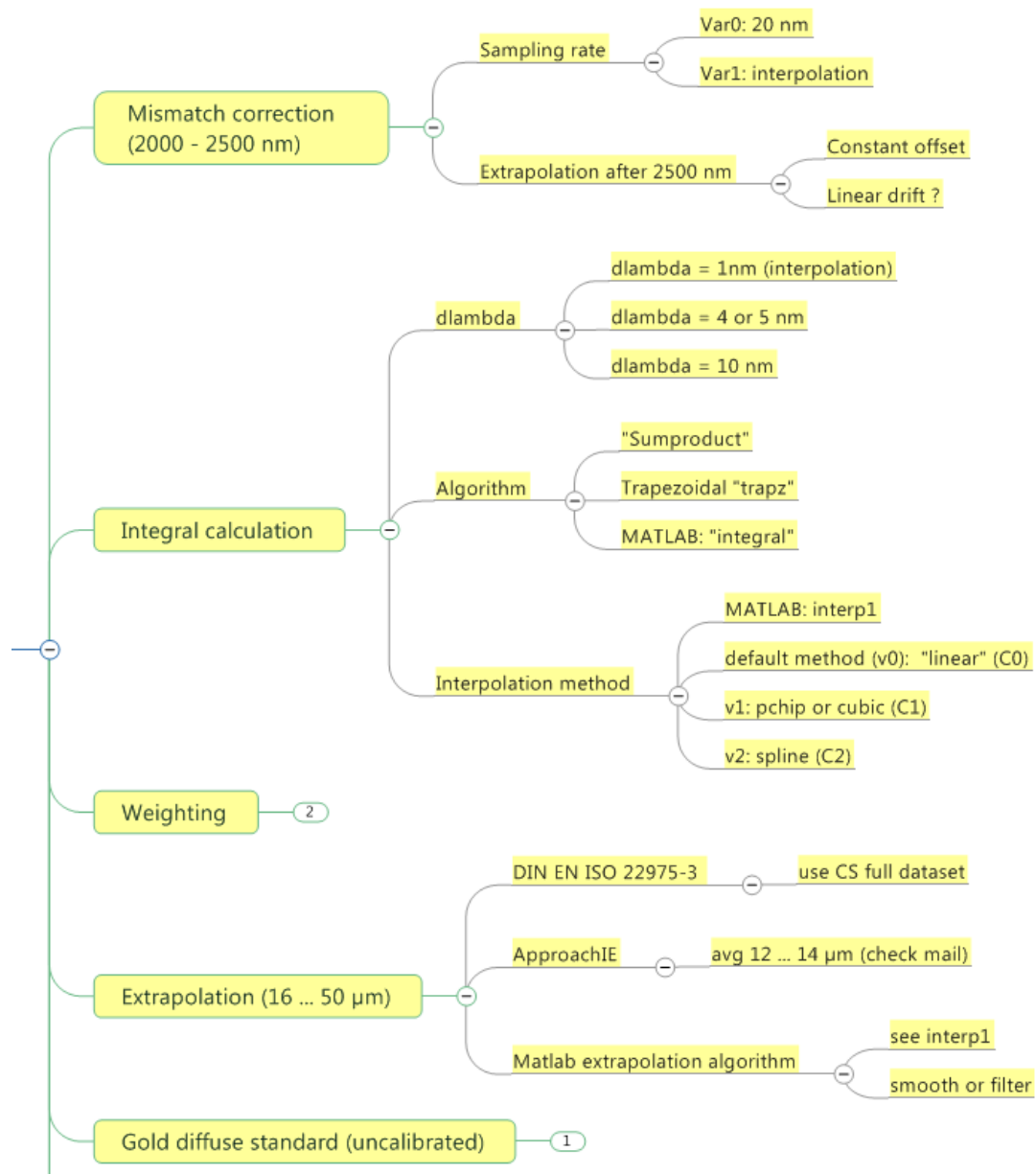


Figure 38 – Detailed view Mindjet MindManager. The branches Mismatch Correction, Integral calculation and Extrapolation have been opened and show the details that need to be considered.

9 Declaration of Academic Honesty / Eidesstattliche Erklärung

I hereby declare to have written the present bachelor thesis on my own, having used no other resources and tools than the listed. All contents cited from published or nonpublished documents are indicated as such.

Hiermit erkläre ich, dass ich die vorliegende Bachelorarbeit selbständig verfasst und keine anderen als die angegebenen Hilfsmittel verwendet habe. Alle Inhalte, die wörtlich oder sinngemäß aus veröffentlichten oder nicht veröffentlichten Schriften entnommen sind, sind als solche kenntlich gemacht.

Place, Date

Signature